Metabolic regulator LKB1 plays a crucial role in Schwann cell-mediated axon maintenance

Bogdan Beirowski[1], **Elisabetta Babetto**[3], **Judith P. Golden**[4], **Ying-Jr Chen**[6], **Kui Yang**[5], **Richard W. Gross**[5], **Gary J Patti**[1,5,6], and **Jeffrey Milbrandt**[1,2]

[1]Department of Genetics, Washington University School of Medicine, St. Louis, MO 63110, USA

[2]Hope Center for Neurological Disorders, Washington University School of Medicine, St. Louis, MO 63110, USA

[3]Department of Developmental Biology, Washington University School of Medicine, St. Louis, MO 63110, USA

[4]Washington University Pain Center, Department of Anesthesiology, St. Louis, MO 63110, USA

[5]Department of Internal Medicine, Division of Bioorganic Chemistry and Molecular Pharmacology, Washington University School of Medicine St. Louis, MO 63110, USA

[6]Departments of Chemistry, Washington University, St. Louis, MO 63110, USA

Summary

Schwann cells (SCs) promote axonal integrity independently of myelination by poorly understood mechanisms. Current models suggest that SC metabolism is critical for this support function and that SC metabolic deficits may lead to axonal demise. The LKB1-AMPK kinase pathway targets multiple downstream effectors including mTOR and is a key metabolic regulator implicated in metabolic diseases. We show through integrative molecular, structural, and behavioral characterization of SC-specific mutant mice that LKB1 activity is central to axon stability, whereas AMPK and mTOR in SCs are largely dispensable. The degeneration of axons in LKB1-mutants is most dramatic in unmyelinated small sensory fibers, whereas motor axons are relatively spared. LKB1 deletion in SCs leads to abnormalities in nerve energy and lipid homeostasis, and increased lactate release. The latter acts in a compensatory manner to support distressed axons. LKB1 signaling is essential for SC-mediated axon support, a function that may be dysregulated in diabetic neuropathy.

Introduction

Axons are extremely long structures with high metabolic demands due to constant ion fluxes, transport of cargoes, and maintenance of their large cell membrane surface area. It is increasingly realized that axon integrity depends not only on neuron-derived provisions but also on support from Schwann cells (SCs) and oligodendrocytes[1,2], the enwrapping glia of the peripheral and central nervous systems (PNS and CNS), respectively. The mechanisms for this non-cell-autonomous support function remain obscure, but emerging evidence indicates that it is distinct from the glial role to insulate axons with myelin[1–3]. Metabolic substrates produced in oligodendrocytes appear to play an essential role in CNS axonal support[4,5], as inhibiting transport of glycolysis-derived carbohydrates (e.g. pyruvate and lactate) from glia to axons results in axonal damage[5]. In accord, mitochondrial respiration in oligodendrocytes was reported to be dispensable for axon integrity as mitochondrial disruption did not cause axonal degeneration as long as glycolytic pathways remained intact[4].

It remains unknown whether metabolic pathways in SCs may be important for axon maintenance in the PNS. Using models of SC mitochondrial dysfunction, we recently implicated abnormalities in the integrated stress response as well as lipotoxic mechanisms in peripheral nerve demyelination with axon loss[6]. A possible impact of aberrant SC metabolism on axon integrity was also observed in another SC mitochondria disruption model characterized by abundant nerve demyelination and neuroinflammation[4].

While these studies attempted to shed light on glial roles in providing axon support, the metabolic control systems in enwrapping glia remain unexplored. Moreover, whether metabolic imbalances that occur in disease similarly affect axonal integrity is particularly significant given the broad association between aberrant metabolism, aging and diverse neurodegenerative conditions with axonal damage. Notably, diabetic neuropathy occurs in association with abnormal glucose and lipid metabolism. Many of the symptoms in this neuropathy result from sensory axon degeneration[7], and it has been proposed that metabolic changes in SCs are involved[8,9]. To examine the glia-axon relationship from this perspective, we sought to identify metabolic regulatory pathways in SCs that are essential for axon maintenance.

The serine/threonine kinase LKB1 (also known as Stk11), and its prime downstream target AMP-activated protein kinase (AMPK), maintain cellular energy homeostasis by regulating key pathways of lipid, carbohydrate, and protein metabolism[10,11]. LKB1 also modulates metabolism independently of AMPK by less-well characterized mechanisms, most notably via multiple AMPK-related kinases[12,13]. In addition to alterations of LKB1-AMPK signaling in metabolic disease and obesity, deregulation of both kinases has been implicated in neurodegeneration including diabetic neuropathy, aging, cancer, and other conditions[10,14,15]. Maintenance of energy homeostasis during cellular stress involves activation of AMPK by LKB1 or alternative upstream kinases to induce catabolism and suppress anabolic processes, to a large part through inhibition of mammalian target of rapamycin (mTOR)[16,17].

To determine whether LKB1-AMPK signaling contributes to glial support of axon integrity, we deleted LKB1 and several downstream targets including the AMPK complex and mTOR in SCs *in vivo*. In support of a crucial role for glial metabolic homeostasis in axon maintenance, we show that SC-specific LKB1 mutants display a pattern of axonal degeneration that is reminiscent of some aspects of diabetic neuropathy. Importantly, similar SC-specific inactivation of AMPK, downstream mTOR kinase as well as further metabolic manipulation in SCs did not result in axon degeneration. Together, our study identifies LKB1 as an important metabolic regulator of SC-derived axonal support, and provides a molecular basis for new glial-centric therapeutic avenues for neuropathies.

Results

Effects of SC-specific LKB1 deletion on nerve development

To study the effects of early LKB1 inactivation specifically in SCs, we bred LKB1$^{fl/fl}$ mice to transgenic mice that express Cre-recombinase (starting from ~E14.5) under control of the P0 promoter. We observed efficient recombination of the floxed LKB1 allele in mutant LKB1$^{fl/fl}$:P0Cre (henceforth termed LKB1-SCKO) nerve genomic DNA, and clear reductions of LKB1 transcript (0.6 +/−0.04-fold lower in qRT-PCR quantification normalized to GAPDH expression; n=3 mice per genotype; p<0.001) and protein levels in P30 sciatic nerves (Fig. 1a,b and Supplementary Fig. 1a,b). LKB1-SCKO mutant mice were born at predicted Mendelian frequency and were normal in weight and size until ~4 months of age (Supplementary Fig. 1c). At older ages, these mutants showed consistent weight decreases (~21%). Nerve conduction velocities in mutant animals at P30 were reduced from 32.14 +/−2.36 m/s (n=7) to 20.31 +/−1.48 m/s (n=8) (p<0.001) without a decrease in compound muscle action potential (CMAP) amplitudes (Supplementary Fig. 2a). This correlated with an early, transient delay in radial sorting and formation of compact myelin at P3–21, which had largely reversed by P30, although g-ratio (axon diameter / myelinated fiber diameter) remained increased (Fig. 1c and Supplementary Fig. 2b,c). SC-differentiation in LKB1-SCKO nerves was impaired as observed by increased numbers of Oct6 and Sox2-positive cells in P21 mutant nerves (Fig. 1d). This was accompanied by significantly reduced levels of the active fragment of axonal neuregulin 1 (Fig. 1e and Supplementary Fig. 2d). In contrast, and likely accounting for the compensatory effects in myelination, we found elevated expression of ERBB2/3 receptors by western blotting of P30 mutant nerve lysates (statistical significance for ERBB3 not reached) (Fig. 1e and Supplementary Fig. 2d). Additionally, mutant SCs strongly expressing Egr2 were more numerous than in control nerves at P21 (Fig. 1d). Despite these alterations in nerve development, primary SC cultures established from P30 LKB1-SCKO sciatic nerves were morphologically indistinguishable from control cultures (Fig. 1f), and we did not observe differences in SC proliferation and cell death (not shown).

LKB1 deficiency can lead to defects in cell polarity[18,19]. However, analysis of longitudinal SC polarization at P60 did not reveal any overt abnormalities in LKB1-deficient nerves (Supplementary Fig. 3). This suggests that, similar to other LKB1-deficient cell types[20–22], ablation of LKB1 in SCs does not cause major polarity defects. Importantly, LKB1-SCKO nerves contained normal numbers of axons at P60 (see below, Fig. 2).

LKB1 deletion in SCs leads to metabolic deregulation

Conditional deletion of LKB1 can be associated with aberrant metabolism and energy depletion[23–25]. To examine if this is also the case for SCs, we performed untargeted metabolomics analysis[26] on sciatic nerve metabolite extracts from P60 mice. The LKB1-SCKO samples differed markedly from control preparations with differential regulation of more than 1,500 metabolic features as defined by unique coordinate pairs of mass-to-charge ratios (m/z) and retention-times (Supplementary Fig. 4). Using model compound databases we tentatively identified 733 dysregulated metabolites (Supplementary Table 1). Lipids were overrepresented including several SC lipid classes such as phospholipids (e.g. phosphatidylcholine (PC) species) and glycolipids (e.g. sulfatides and cerebrosides)[27]. Moreover, we observed changes in concentrations of amino acids/small peptides as well as elevated lactate levels in LKB1-SCKO preparations (lactic acid; KEGG: C01432; 2.66-fold up-regulated; p=0.000208).

We next measured AMP and ATP concentrations in sciatic nerve preparations. This demonstrated relatively constant AMP/ATP ratios in control nerves from P30 onwards. In contrast, gradual ATP depletion in LKB1-SCKO nerves resulted in progressively increasing AMP/ATP ratios (Fig. 2a). This energy deprivation was accompanied by an age-dependent decrease in NAD^+/NADH ratios, driven by significant elevations in NADH levels while NAD^+ concentrations remained constant (Fig. 2b,c). Importantly, SC numbers in LKB1-SCKO nerves were indistinguishable from control nerves, with no evidence of increased SC apoptosis (Supplementary Fig. 5a–d). These studies indicate that SCs from LKB1-SCKO mutant nerves with metabolic dysregulation are energetically deficient, possibly secondary to defects in oxidative phosphorylation as observed in other LKB1 deficient cell types[23–25].

LKB1-SCKO mutants develop progressive axonopathy

We next studied the consequences of dysregulated SC metabolism on nerve integrity. A subset of LKB1-SCKO mutants (~10%) started to develop significant neurological abnormalities (e.g. unsteady gait and hindlimb clasping) indicative of peripheral neuropathy by P90. The abnormalities progressively worsened with age, such that all 12-month-old mutants showed signs of neuropathy (Supplementary Fig. 5e). A number of 18-month-old mutants displayed severe ambulatory impairment but did not have overt muscle paralysis (Supplementary Video 1).

Degeneration of myelinated and unmyelinated axons became initially apparent in P90 LKB1-SCKO sciatic and femoral nerves (Fig. 2d,e, and not shown). The fiber degeneration gradually progressed (Fig. 2j–m,p) and was especially prominent for unmyelinated axons (Fig. 2h,i,n,o,q). Remarkably, nerves from many 12–18-month-old mutant mice were almost completely devoid of unmyelinated axons (Fig. 2j–o). The degeneration was further examined using LKB1-SCKO mice with neuronal yellow fluorescent protein (YFP) expression, which showed axonal fragmentation and swelling, that was accentuated in aged mice (Fig. 2f,g and Supplementary Fig. 5f). The axon loss was accompanied by reduced nerve size with higher density of SCs (Supplementary Fig. 5g,h).

We then tested if the developmental defects could account for the axon degeneration. To this end we utilized an inducible PLP-Cre[ERT] allele to ablate LKB1 in adult myelinating and non-myelinating SCs after tamoxifen injections starting at P30. We observed efficient recombination of the floxed LKB1 allele and reduced LKB1 protein levels in tamoxifen treated LKB1^{fl/fl}: PLP-Cre[ERT] (LKB1-iSCKO) nerves (Supplementary Fig. 6a,b). Whereas age-matched vehicle treated LKB1^{fl/fl}: PLP-Cre[ERT] and tamoxifen treated LKB1^{fl/fl} control mice exhibited no abnormalities, 12-month-old LKB1-iSCKO mutants showed abnormal gait, ambulatory deficits, and ataxia (Supplementary Videos 2–3 and Supplementary Fig. 6c). Morphological analysis of sciatic nerves from these mutants demonstrated many collapsed myelinated fibers (Fig. 3a–d), marked disintegration of unmyelinated axons (Fig. 3e,f), and significant reductions in overall axon numbers (Fig. 3g,h). Importantly, these degenerative events were not preceded or accompanied by structural changes in the myelin of intact axons (Supplementary Fig. 6d–f). Indeed, nerve conduction velocities were normal in LKB1-iSCKO mutants 3 and 10 months following tamoxifen administration (Supplementary Fig. 6g). These results demonstrate that LKB1 function in SCs is required for axon maintenance in adulthood after nerve development is completed, whereas its function is dispensable for SC myelin maintenance. In conclusion, LKB1 in SCs is essential for the preservation of both unmyelinated and myelinated axons independently of myelination.

Preferential loss of sensory axons in LKB1-SCKO mutants

Although we observed substantial axon loss in adult LKB1-SCKO mutants, there was a distinct absence of overt motor symptoms. We performed assays for motor function and found no significant deficits in aged LKB1-SCKO mice (Supplementary Fig. 7a,b). There were deficits in the rotarod test, but only in mutant mice older than 12 months of age (Supplementary Fig. 7c). In the absence of reduced muscle strength, we surmised that these abnormalities could be due to defects in coordination or tactile sensory defects, or both. However, pole climb and turn tests, which measure coordination, were also normal in aged mutants (Supplementary Fig. 7d). Consistent with the relative preservation of the motor system, no overt macroscopic or microscopic abnormalities in muscles were observed in 12 and 16-month-old mutants (Supplementary Fig. 7e,f), in sharp contrast to other metabolic neuropathy models[4,28]. Moreover, there were no electrophysiological signs of muscle denervation, significant changes in proximal and distal motor axon numbers, or axon terminal abnormalities at neuromuscular junctions of peripheral muscles in aged LKB1-SCKO mice (Fig. 4a,d, Supplementary Fig. 8a–e, and not shown). However, in quadriceps nerves (predominantly motor) of 18-month-old mutants we did observe reduced numbers of myelinated axons indicating that motor axons are not completely resistant to the changes elicited by LKB1 loss (Supplementary Fig. 8f).

In contrast to the relative sparing of the motor system, the deterioration of unmyelinated fibers as noted by the progressive degeneration of Remark bundles was accompanied by multiple sensory deficits already in young animals. First, we found dramatic reductions of intraepidermal sensory terminals (C-fibers) in hind paws from LKB1-SCKO mice (Fig. 4b). Loss of these skin nociceptor afferents results in defects in temperature sensitivity. In accord, hot-plate and Hargreaves tests revealed progressively longer reaction latencies

indicating reduced sensitivity to noxious heat stimuli in these mutants (Fig. 4c and Supplementary Fig. 9a). These deficits correlated well temporally with the degeneration of Remak bundles in LKB1-SCKO nerves (Fig. 2q). We also observed significant abnormalities in the acetone and cold-plate tests (unmyelinated and thinly myelinated Aδ fibers), and smaller changes in von Frey mechanical sensitivity testing (myelinated Aβ fibers) (Supplementary Fig. 9b,c, and not shown). To correlate these behavioral findings with structural data, we analyzed peripheral nerves containing predominantly sensory axons, and spinal cord dorsal roots. Indeed, quantification of myelinated fibers in saphenous and sural nerves as well as L3 dorsal roots demonstrated significantly decreased axon numbers in 12-month-old or older mutants, but not at P45 (Fig. 4e, Supplementary Fig. 9d,e, and not shown). This axon degeneration was not secondary to neuronal death, as overall numbers of L3 DRG neurons that project to these sensory nerves were indistinguishable between the groups (Supplementary Fig. 9f). Together these results prompted us to hypothesize that loss of LKB1 activity in SCs induces preferential destabilization of small diameter fibers. We thus performed quantitative fiber morphometry in young and aged mice. While we did not detect significant distribution differences in P90 mice (Supplementary Fig. 9g), this analysis revealed that the percentage of small axons of 1–2 μm diameter was significantly reduced in 8-month-old LKB1-SCKO nerves (Fig. 4f).

In sum, these results provide strong evidence that the axonopathy in LKB1-SCKO nerves primarily affects small diameter fibers, including the unmyelinated axons organized into Remak bundles as well as myelinated sensory axons.

Axon loss is not due to demyelination and inflammation

Nerve demyelination and neuroinflammation as mechanisms for axon damage[1,3] were not apparent in LKB1-SCKO nerves, in accord with the data from LKB1-iSCKO mutants in which axon degeneration occurred independently of changes in myelination. First, histological signs of chronic demyelination (e.g. onion bulb formation) were not observed in mutant nerves. Second, serial g-ratio measurements showed a gradual increase in myelin thickness in LKB1-SCKO nerves over time rather than a progressive myelin thinning (Fig. 5a, b and Supplementary Fig. 10a). Third, levels of major structural myelin proteins suggested conserved or even slightly improved myelin integrity in older mice (Fig. 5c). Fourth, we did not detect overt macrophage and T-lymphocyte invasion in peripheral nerves by electron microscopic inspection, and no significant increases in Iba1, CD68, or CD3 immunolabeling in 12-month-old LKB1-SCKO mice (Supplementary Fig. 10b–d). Finally, there was no temporal dispersion in individual CMAP traces (Fig. 5d) or deterioration in nerve conduction velocity throughout the neuropathy (Fig. 5e), findings that are inconsistent with progressive demyelination.

The mouse vagus nerve is composed predominantly of unmyelinated axons, which showed dramatic degeneration in aged LKB1-SCKO mutants (Fig. 5f). This indicates that unmyelinated vagal axons degenerate as a consequence of the metabolic perturbation in the LKB1 mutant non-myelinating SCs, and degeneration is not caused by demyelination.

Additional evidence that axon degeneration is not associated with demyelination in LKB1-SCKO nerves came from examination of longitudinal polarization of mutant SCs from aged

mice. SC polarization defects occur in demyelinating neuropathies including abnormalities in the morphology of nodal and internodal areas of non-compact myelin[(e.g. 6)]. Imaging of teased fiber preparations from aged LKB1-SCKO mutants expressing enhanced green fluorescent protein (EGFP) in SCs demonstrated that the overall configuration of the cytoplasmic network and SC polarity at internodes and nodes was normal (e.g. normal arrangement of Schmidt-Lanterman incisures and Cajal bands) (Fig. 5g), similar to the normal SC polarity observed in younger mutant mice before the onset of axon degeneration.

To gain more mechanistic insight into why these mutant SCs cannot provide adequate axonal support, we performed microarray analysis using nerve mRNA from P60 mice, an age immediately prior to the initiation of axonal loss (Supplementary Table 2). Transcripts of major regulators of PNS myelination (e.g. Nrg-1, ErbB2/3, Egr2) as well as those encoding structural myelin proteins and key nerve inflammatory markers (e.g. CSF-1, MCP-1) were normal in LKB1-SCKO nerves. Some notable exceptions included the down-regulation of Lgi1, and the up-regulation of chemokine ligands 4/14, and interleukin 10 receptor α, respectively. Curiously, but compatible with reported LKB1 deletion phenotypes[29], transcripts involved in melanin biosynthesis (e.g. premelanosome protein Pme1, tyrosinase-related protein 1) were strongly up-regulated in LKB1 depleted nerves. Moreover, we found aberrant regulation of transcripts implicated in lipid metabolism (e.g. down-regulation of squalene epoxidase, up-regulation of acyl-CoA thioesterase). Notably, the profiling revealed induction of multiple genes encoding proteins collectively characteristic of de-differentiated SCs and of the SC response to axon injury[30] (i.e. *Pou3f1/ Oct6; Gdnf; Sox4; Shh; tenascin C; cyclin D1; Ki67, CD44; coronin; Integrin α3; Protein tyrosine phosphatase, receptor type; TNFR superfamily member 12a; Tcfap2a*), as well as injury-associated nerve tissue remodeling[30] (i.e. *MMP17; Ptprt; Ela1; Klk10; Hapln2; Klk8*). In accordance, LKB1-deficient SCs displayed elevated expression of c-Jun, a hallmark regulator in de-differentiated SCs associated with axon injury[31] (Supplementary Fig. 11). Thus, prior to the actual onset of axon loss the LKB1-deficient SCs display a number of transcriptional changes reminiscent of the expression pattern associated with the SC axon injury response. It should be noted that some of the observed changes could also reflect delayed SC development in LKB1-SCKO nerves (see above).

LKB1 effects are independent of abolished AMPK/mTORC1

The axon degeneration in LKB1-SCKO mutants could result from abolished AMPK activation in SCs due to LKB1 loss, as LKB1 is often described as the major upstream kinase of AMPK[11]. The elimination of AMPK activity, in turn, leads to augmented mTOR complex 1 (mTORC1) activity largely via reduced phosphorylation of tuberous sclerosis complex 2 (TSC2), the major inhibitor of mTORC1, and induction of Raptor, a critical component of mTORC1 complex[16,17,32]. Rapamycin, a drug that inhibits primarily mTORC1 signaling, can reverse some of the pathology observed following LKB1 ablation in other systems[10,19,21,33,34]. Given these observations, along with the apparent role of glial mTOR signaling in regulation of peripheral myelination[35], we assessed the impact of pharmacological mTORC1 inhibition on the LKB1-SCKO axon phenotype. First, to validate our rapamycin treatment regime we utilized SC-specific phosphatase and tensin homolog (PTEN) knockout mice (PTEN^{fl/fl}:P0Cre; PTEN-SCKO). These mutants display

dysregulated mTORC1 signaling through AKT overactivation leading to exuberant myelin growth and subsequent PNS axon degeneration (Fig. 6a), similar to recently reported results from PTEN^{fl/fl}-CNP1Cre mutants[36]. Remarkably, rapamycin treatment from P30–90 had salutary effects on overall nerve integrity and resulted in dramatic axon protection in PTEN-SCKO mice (Fig. 6a, and unpublished observations). In sharp contrast, the identical treatment regime had no effect on axon integrity in LKB1-SCKO mutants (Fig. 6a, b).

In addition, we quantified axon numbers in peripheral nerves from SC-specific mTOR mutants (mTOR^{fl/fl}:P0Cre; mTOR-SCKO) and did not observe loss of myelinated or unmyelinated axons during aging, despite substantial myelination deficits and other nerve defects in these mutants (Supplementary Fig. 12). Therefore, deregulation of the mTORC1 pathway in SCs does not underlie the axonal phenotype observed in LKB1-SCKO mutants.

The primary metabolic target of LKB1 is AMPK. To determine if abolished AMPK activity in SCs could phenocopy the axonopathy in LKB1-SCKO mutants we generated SC-specific AMPK knockout mice. To ensure complete inactivation of the AMPK complex in SCs, two sets of mutants were generated with either complete ablation of all β-subunit isoforms (AMPKβ1/2-SCKO) or all α–subunit isoforms (AMPKα1/2-SCKO) in SCs (Supplementary Fig. 13a,b). Contrary to the hypothesis that failed AMPK activity in SCs mediates the axonal effects following LKB1 ablation, both AMPKβ1/2-SCKO and AMPKα1/2-SCKO mutants displayed no apparent neurological abnormalities or behavioral defects (in a battery of motor and sensory tests) from birth to at least 12 months of age (Supplementary Fig. 13c,d, and not shown). Nerve morphometry and electron microscopy showed a normal axon structure in these mutant mice (Fig. 6c, and not shown). The numbers of myelinated and unmylinated axons in sciatic nerves from AMPKβ1/2-SCKO mice were normal at an early age through 18 months of age, although we did observe progressive hypomyelination (Fig. 6c–e, and Supplementary Fig. 14a). Similar results were obtained from AMPKα1/2-SCKO mice (Supplementary Fig. 14b–d, and not shown).

Hence, while AMPK is often the primary effector of LKB1 metabolic actions, it does not play an essential role in SC-mediated axonal support functions.

LKB1 deletion results in profound metabolic changes

The absence of axonopathy in AMPK-deficient mice prompted us to examine if AMPK was inactivated in LKB1-SCKO mutants *in vivo*. Surprisingly, we found increased AMPKαT172 phosphorylation (an established indicator for AMPK activation) in P30 LKB1-SCKO nerves (Fig. 7a). This is consistent with the observed energetic depletion in LKB1-SCKO nerves and suggests that AMPK can be activated via non-LKB1 dependent mechanisms in SCs[11,37]. Two alternative upstream kinases, the Ca^{2+}/calmodulin-activated protein kinase kinase (CaMKK) and the MAP3 kinase Tak1 (MAP3K7, TGF-β-activated kinase-1), can activate AMPK independently from LKB1 in non-canonical pathways[38–40]. We thus studied their activation level and found no changes in CamKK signaling but a strong activation of Tak1 (phosphorylation at Thr184/187) in LKB1-SCKO nerves (Supplementary Fig. 15a–c), indicating that Tak1 may phosphorylate AMPK in the absence of LKB1.

Activated AMPK is a negative regulator of lipid anabolism via targets such as Acetyl-CoA Carboxylase (ACC; fatty acid synthesis and oxidation) and 3-hydroxy-3-methylglutaryl-CoA reductase (HMGR; cholesterol synthesis)[11]. In accord with abnormalities in lipid metabolism detected in our metabolomics analysis, LKB1-SCKO nerves showed increased phosphorylation of ACC (phospho-Ser79) (Fig. 7a). Correspondingly, we found reduced levels of cholesterol, triglycerides, and fatty acids in mutant nerves, although only cholesterol levels showed statistically significant differences at every age studied (Fig. 7b, and not shown). Moreover, in a mass-spectrometry-based shotgun lipidomics approach using nerve lipid preparations from P60 mice, we detected reduced levels (~35%) of major myelin lipids including phospholipids (total phosphatidylethanolamine with its subspecies) and glycolipids (total cerebroside with its subspecies) (Fig. 7c and Supplementary Table 3). Thus, LKB1 loss unexpectedly leads to induced AMPK activity and to inhibition of SC lipid synthesis (especially cholesterol) prior to axon loss.

AMPK activation also negatively regulates protein synthesis and cell growth through phosphorylation of both TSC2 and Raptor[17,32]. In addition to slightly increased TSC2 and Raptor phosphorylation we observed an overall attenuation of the protein synthesis pathway in P30 LKB1-SCKO nerves as reflected by decreased phosphorylation of the mTORC1 downstream targets ribosomal S6 kinase, S6 ribosomal protein, and eukaryotic initiation factor 4E-BP1 (Fig. 7a). The reduced mTORC1 activity is consistent with the reduced nerve and SC size in LKB1-SCKO mice.

LKB1-AMPK signaling controls mitochondrial biogenesis and turnover through regulation of PGC1α and ULK1/2[11]. Alterations of mitochondrial load and function have been reported following LKB1 elimination[23,25,41]. In agreement, LKB1-SCKO nerves showed elevated PGC1α levels with a dramatic increase in the mitochondrial proteins TFAM and VDAC (porin) (Fig. 7d). Total mitochondrial numbers as well as the cumulative mitochondrial membrane potential were increased in SCs from mutant mice (Fig. 7e and Supplementary Fig. 16a). Given the progressive energetic depletion in mutant nerves (Fig. 2a), this likely reflects a compensatory expansion of mitochondria secondary to mitochondrial dysfunction. Consistent with this dysfunction, we observed increased enzymatic cytochrome oxidase (COX) labeling in young LKB1-SCKO nerves whereas none was noted in aged nerves (Fig. 7f) despite a progressive increase in mitochondrial content (Supplementary Fig. 16b). This temporal readout of mitochondrial function in relation to mitochondrial load and increased phosphorylation of the mitophagy regulator ULK1 (Fig. 7d) indicates that mitochondrial homeostasis in LKB1-deficient SCs is abnormal. To further examine whether there are direct detrimental consequences of the mitochondrial dysfunction we assessed mitochondrial reactive oxygen species (ROS) production in isolated SCs from young and aged mice (measured by MitoSOX Red biosensor incorporation). We found a slight but significant increase of mitochondrial ROS in LKB1-deficient SCs isolated from 12-month-old mutant nerves as compared to cells from age-matched control mice (Fig. 7g). Together with the important role of mitochondrial homeostasis in maintenance of nerve integrity these data suggest the possibility that mitochondrial misregulation in SCs contributes to axonal destabilization in LKB1-SCKO mutants.

Based on our metabolomics screen and the importance of lactate in maintaining neuronal compartments in the CNS, we next explored the effects of LKB1 loss on SC glucose regulation. The LKB1-AMPK pathway controls glycolysis via cellular glucose uptake and regulation of glycolytic enzymes[11,14]. Lactate concentrations were increased in sciatic nerves of LKB1-SCKO mice starting at P90 (Fig. 8a), which coincides with the onset of axon degeneration. This was associated with increased lactate dehydrogenase (LDH) enzymatic activity in mutant nerves (Fig. 8b). Interestingly, we did not detect significant differences in the expression levels of a number of key glycolytic enzymes or carbohydrate transporters in LKB1-SCKO nerves and LKB1-deficient SCs (Supplementary Fig. 17a–d, and not shown). We also observed no differences in total nerve glucose levels at any age studied (Supplementary Fig. 17e). To test if LKB1-deficient SCs release increased amounts of lactate, we cultured control and LKB1-SCKO sciatic nerve explants and measured lactate concentrations in the culture media after 48 hr of incubation. The mutant nerves released significantly higher amounts of lactate (6.34 +/−0.23 mM lactate in culture media; N=3 mice) than control nerves (4.15 +/−0.28 mM lactate; N=3 mice) (p=0.004), suggesting that peripheral axons in mutant nerves are exposed to increased lactate concentrations.

Increased lactate levels in mutant nerves support axons

The increased lactate release in LKB1-SCKO nerves raised the question as to whether this is detrimental (by causing tissue acidosis) or beneficial (by providing energy substrate) for axon integrity. In variance with adverse lactate effects, incubation of primary dorsal root ganglion (DRG) axon cultures with increasing concentrations of lactate in the media did not elicit any apparent axonal degeneration (Supplementary Fig. 18a). To explore the role of aberrant nerve lactate levels for axon integrity *in vivo*, we attempted to reduce lactate production in LKB1-SCKO mutants. P30 mutants were treated with 2DG (a glucose analog that inhibits glycolysis) for 60 days, and the effects on axon survival in sciatic nerves were quantified. Importantly, the 2DG treatment regime had no significant effects on overall behavior or body weight in LKB1-SCKO mice (Supplementary Fig. 18b,c). However, 2DG treatment did normalize nerve lactate levels in LKB1-SCKO nerves from 5.25 +/−0.19 mM (n=7, vehicle treated) to 3.64 +/−0.30 mM (n=11) (p=0.019) by P90, so that no differences in nerve lactate concentration were detectable between treated mutant and control mice (vehicle treated control: 4.18 +/−0.30 mM (n=7); 2DG treated control: 3.41 +/−0.50 mM (n=11). We found that 2DG administration slightly but significantly exacerbated axon loss in P90 LKB1-SCKO sciatic nerves whereas it had no effect in control animals (Fig. 8c,d). If the increased lactate was toxic to the axons, then lowering lactate with 2DG should have reduced the amount of axonal loss; instead axon losses increased suggesting the increased lactate reflects a compensatory response by the SC, and an attempt to provide additional support to the deteriorating axons.

Discussion

This study shows that LKB1 is a crucial regulator of major metabolic pathways in SCs that are central to their role in supporting axonal integrity. LKB1-deficient SCs display multiple metabolic abnormalities, some of which may reflect alterations in AMPK and mTOR activity. However, the loss of axon maintenance functions in LKB1-deficient SCs is largely

independent of AMPK and mTOR signaling. These findings are particularly intriguing in view of the fact that abnormalities in this pathway have been implicated in metabolic pathologies, aging, and neurodegeneration. Furthermore, these studies separate SC axon support functions from their more widely appreciated role in myelination.

In contrast to other neuropathy models the axon degeneration in the LKB1 mutants is not due to demyelination and inflammation. This strongly suggests that axon degeneration is a direct result of perturbed bioenergetics and metabolic support by SCs. Since axon degeneration is a hallmark of many neuropathies, our study opens the possibility that metabolic misregulation in SCs linked to altered LKB1 signaling may be an important contributor to axon loss in these disorders, and especially in those associated with aberrant metabolism.

LKB1 deletion in SCs leads to energetic depletion, mitochondrial dysfunction, and widespread alterations in nerve redox state, lipid metabolism, enzymatic activities, and increased lactate levels. It is likely that many of these alterations reflect contributions from additional AMPK-related kinases (i.e. other than AMPK) that are also associated with LKB1 metabolic functions[12,13,42,43]. Our finding that complete loss of AMPK activity in SCs is not harmful to axons indicates that abnormal AMPK signaling in SCs is unlikely to be the predominant underlying factor leading to axonal loss, thus implicating glial AMPK-related kinases or other LKB1 targets in axon maintenance. Suppression of mTOR signaling likewise does not result in axonal degeneration, as aged SC-specific mTOR mutants have normal axon numbers and rapamycin administration in LKB1-SCKO mutants had no effect on axon stability. These data indicate that metabolic changes in LKB1-deficient SCs, which are largely independent of AMPK and mTOR, must be responsible for the axon degeneration in these mice. Indeed, these SC axonal support modalities are needed continually for proper axon maintenance, as inducible deletion of LKB1 in SCs in adult mice leads to a dramatic axonal loss. We thus propose that LKB1, together with specific downstream substrates, provides the appropriate balance of multiple metabolic pathways that ultimately leads to long-term support of axon integrity. Future studies will have to elucidate which pathways downstream of LKB1 and its substrates play important roles here.

Each of the characterized metabolic changes in mutant SCs separately, or in combination, may contribute to axonal loss. Because glial lactate provides support for CNS axons[4,5], we sought to determine the role of elevated lactate levels in LKB1-depleted nerves. We found that abolishing the increased lactate production from these mutants SC results in further axon pathology. This demonstrates that glial release of lactate also supports axon integrity in the PNS, and extends this function to pathological situations where it appears to be a compensatory response aimed at sustaining distressed axons. Notably, increased nerve lactate levels also have been observed in rodent models for diabetic neuropathy[44,45]. Thus, it will be interesting to explore the role of lactate on axon integrity also in these models.

Despite LKB1 elimination, mutant SCs *in vivo* appear to respond with robust activation of AMPK. This surprising effect has also been observed in other LKB1-deficient cells[18,38], but remains poorly understood. The strong activation of Tak1 signaling in LKB1-SCKO nerves suggests that Tak1 acts as an upstream kinase for AMPK[39,40] in SCs under stress conditions.

How Tak1 is activated in LKB1-deficient cells is unclear, but may involve sensing the energetic deficits in these cells. In LKB1-SCKO nerves, some of the compensatory effects, like increased lactate release through enhanced glycolysis, are likely the direct consequence of AMPK activation in LKB1-SCKO nerves.

Despite the axon demise in tamoxifen-inducible LKB1-iSCKO mice there were no changes in myelination in these mutants except the focal myelin breakdown as a direct consequence of axon degeneration. This suggests that LKB1 in adult SCs is dispensable for the maintenance of compact myelin once it is formed, which is consistent with the lack of demyelination in the LKB1-SCKO mutants (although LKB1-SCKO mutants show delayed SC maturation and developmental myelination likely due to the metabolic dysregulation). The exclusion of demyelination as etiological factor for the axonopathy in LKB1-SCKO mice is perhaps surprising given the alterations in lipid metabolism and aberrant mitochondrial homeostasis. Recently, we mechanistically linked a demyelinating neuropathy resulting from SC mitochondrial dysfunction (Tfam-SCKO mutant) to aberrant lipid metabolism and to activation of the integrated stress response[6]. In particular, we proposed that reduction of myelin-enriched lipids (sulfatides and cerebrosides) and accumulation of detrimental acylcarnitine species in Tfam-SCKO nerves contribute to nerve demyelination with subsequent axon loss. Our lipidomics screen revealed normal levels of acylcarnitines in LKB1-SCKO nerves (Supplementary Table 3), excluding a similar lipotoxic mechanism. Instead, it is possible that the low levels of various myelin lipids in LKB1-SCKO mice are secondary to increased AMPK activity leading to attenuation of energy-costly lipid synthesis. In agreement, our microarray analysis revealed early and significant down-regulation of squalene epoxidase, a central and rate-limiting step in cholesterol[46] and thus myelin synthesis.

The preferential degeneration of small diameter unmyelinated afferents in LKB1-SCKO mutants and relative sparing of large caliber motor axons calls for a comparison to acquired human neuropathies, especially those associated with diabetes, obesity, and aging. The most common and incapacitating symptoms in these conditions (i.e. pain, paresthesias) are those associated with small-fiber degeneration, whereas large motor fibers are relatively spared. The underlying mechanisms accounting for the high vulnerability of small-diameter axons in these conditions are unexplained. Although various hypotheses have been proposed[47–49], the potential contribution of SC abnormalities to this vulnerability has not been appreciated. Furthermore, LKB1-SCKO mice also manifest extensive axon degeneration in the vagus nerve that contains mostly small parasympathetic fibers, mimicking an important feature of autonomic diabetic neuropathy[50]. Although diabetic polyneuropathy is certainly a multifactorial disorder, our discovery that metabolic dysregulation in SCs triggers primarily small fiber degeneration may help to limit the number of potential underlying mechanisms and put new emphasis on the SC as a pathophysiologic target. This selective loss could reflect a greater dependence of small unmyelinated axons on SC bioenergetic support[3]. Alternatively, it is conceivable that their instability arises from accumulation of harmful metabolites, which would lead to much higher concentrations in small axons due to their lower axoplasm volume. The discrimination of such mechanistic scenarios will require future work and will need to incorporate measurements of metabolic and other changes in the axon directly through metabolic sensors and other modalities.

Methods

Generation of SC-specific mutant mice

All animal experiments were reviewed and approved by the Washington University Animal Studies Committee (protocol approvals #20110071 and 20140044). LKB1-SCKO mutants and control littermates were generated by crossing LKB1^{fl/fl} mice[52] (FVB) to P0-Cre transgenic mice[53] (C57BL/6). LKB1-SCKO mutants were additionally crossed to Thy1.2-YFP-16 mice[54] and PLP-EGFP transgenic mice[55] (both C57BL/6) for fluorescent axon and SC imaging, respectively. For SC-specific LKB1 ablation in adult animals (LKB1-iSCKO), LKB1^{fl/fl} mice were crossed to PLP-Cre[ERT] transgenic mice[56] (C57BL/6).

Following mutant mouse strains were obtained from the European Conditional Mouse Mutagenesis programme (EUCOMM) and Knockout Mouse Project (KOMP) (Wellcome Trust Sanger Institute, Mouse Genetics Programm): B6N; B6N-Mtor[tm1a(EUCOMM)Wtsi] (for mTOR deletion); B6N; B6N-Prkab1[tm1a(KOMP)Wtsi] (for AMPKβ1 deletion) (both C57BL/6). mTOR^{fl/fl} and AMPKβ1^{fl/fl} mice were generated by crossing these mutant mouse strains to germ cell-expressing Flp recombinase transgenic mice[57] (C57BL/6) in order to deactivate the 'knockout-first allele' promotorless cassette (containing splice acceptor, βgal, neo, and pA signal for constitutive knockout).

mTOR-SCKO mutants were generated by crossing mTOR^{fl/fl} mice to P0-Cre transgenic mice. For generation of AMPKβ1/2-SCKO mutants, AMPKβ1^{fl/fl} mice were crossed to Bay Genomics gene-trap AMPKβ2 deficient mutants[58] (C57BL/6) and P0-Cre transgenic mice. For generation of AMPKα1/2-SCKO mutants, AMPKα2^{fl/fl} mice[59] (C57BL/6) were crossed to AMPKα1 mutants[60] (C57BL/6) and P0-Cre transgenic mice. PTEN-SCKO mutants were generated by crossing PTEN^{fl/fl} mice[61] (C57BL/6) to P0-Cre transgenic mice. Genotyping for all mutants was performed by PCR strategies using standard procedures and appropriate primers (sequences available upon request).

Tamoxifen, rapamycin, and 2DG treatment of mice

Intraperitoneal injections of tamoxifen (Sigma; daily 180 μg per gram mouse weight) and rapamycin (LC Laboratories, daily 10 μg per gram mouse weight) were performed similar to previously reported procedures[36,62].

2-deoxy-D-glucose (2DG) (Sigma) was dissolved in physiological saline to a final concentration of 40 mg/ml. P30 mice received daily intraperitoneal injections (Monday-Saturday) at 500 μg 2DG per gram mouse weight (or only the carrier solution as control).

Histology of nerves and muscles

Processing of samples for generation of semithin and ultrathin nerve sections was performed as described previously[51,63]. Hematoxylin and eosin staining of mouse muscle sections was performed using standard procedures. Preparation and imaging of tibial nerve teased fibers from mice expressing the *PLP-EGFP* transgene was performed as reported previously[63].

Confocal imaging of YFP or EGFP-labelled whole-mount nerve and muscle preparations, and skin intra-epidermal fibers

For analysis of YFP-labelled axons or EGFP-labelled SCs in whole-mount nerve preparations from mice expressing the *Thy1.2-YFP-16* or *PLP-EGFP* transgenes, ~1.5-cm-long sciatic nerve segments were dissected, processed and imaged as previously described[64].

Neuromuscular junctions (NMJs) and intramuscular nerve fibers in fixed flexor digitorum brevis (FDB), extensor halluces longus (EHL), and lumbrical muscles from mice expressing the *Thy1.2-YFP-16* transgene were visualized by staining of acetylcholine receptors with tetramethylrhodamine isothiocyanate conjugates of α-bungarotoxin (TRITC-α-BTX) (Biotium). Muscle preparations were mounted on glass slides in Vectashield mounting medium for subsequent confocal or wide-field epifluorescence imaging. Total numbers of intact NMJs were counted in whole-mount preparations of EHL muscles applying previously reported criteria[51]. NMJs in both limb muscles of each experimental animal were quantified.

For imaging of intra-epidermal axon terminals in mice expressing *Thy1.2-YFP-16*, skin biopsies were collected from hind-paws, immersion-fixed in Zamboni fixative, and embedded in OCT media for production of frozen sections. Confocal imaging was used for visualization of YFP-labelled intra-epidermal axon terminals.

Quantification of myelinated and unmyelinated axons in peripheral nerves

We performed counts of intact axons in sciatic, quadriceps, saphenous, and sural nerves as well as ventral/dorsal spinal cord roots on high-magnification semithin micrographs using established non-biased counting methods[51,64,65]. The ImageJ software cell-counter plug-in and calibrated area measurements were used for axon quantification. For manual quantification of myelinated fiber numbers in sciatic nerves we counted axons in at least 4 randomly selected images of the sciatic nerve transverse section (each 6000 μm^2). Total numbers of axons in the whole nerve were extrapolated based on the total area of the nerve. For facilitated quantification of unmyelinated axons in Remak bundles in sciatic nerves, we calculated the area occupied by preserved unmyelinated axon bundles in at least 4 randomly selected images of the sciatic nerve section (each 6000 μm^2). The total area of unmyelinated axon bundles in each transverse nerve sections was calculated by interpolation. For quantification of myelinated fibers in quadriceps, saphenous and sural nerves as well as ventral/dorsal spinal cord roots, all axons on each transverse section were counted. Counts were carried out by a masked investigator (B.B. or E.B.).

Calculation of g-ratios and quantitative histomorphometry

G-ratios of individual myelinated axons in sciatic nerves as a measure of myelin thickness were determined using a plugin for the ImageJ software which allows semi-automated analysis of randomly selected axons on nerve transverse sections (http://gratio.efil.de). Using 4 randomly selected semithin light micrographs (each 6000 μm^2) per sciatic nerve section from each analyzed mouse, we performed measurements on a total of 100 randomly chosen fibers. Cumulative g-ratios were calculated for each mouse by averaging all individual g-ratios.

Fiber size distribution morphometry was carried out using an automated digital imaging system and custom-made morphometry software (Leco IA32, Leco Instruments) as described previously[63,66].

Immunofluorescence and cell quantifications

Dissected sciatic nerves were immersion fixed in 4% PFA/PBS for 1–24 hrs, cryoprotected in 30% sucrose, and embedded in Tissue-Tek OCT compound (Sakura Finetek). Immunofluorescence on longitudinal and transverse frozen nerve sections including TUNEL staining was performed as described previously[28,63]. DAPI-positive SC nuclei, and TUNEL-, Iba1-, CD68-, and CD3-positive cells were quantified on entire transverse sciatic nerve sections. Counts were carried out by a masked investigator (B.B.).

Nerve cytochrome oxidase staining

Sciatic nerves from control and LKB1-SCKO mutant mice were freshly dissected, placed in Tissue-Tek OCT compound, and immediately frozen. An incubating solution containing 75 mg/ml sucrose, 0.5 mg/ml 3,3′-diaminobenzidine tetrahydrochloride 2 (DAB, 0.6 mg/ml), 2 μg/ml catalase (from bovine liver), and 1mg/ml cytochrome c in 0.05 M sodium phosphate was placed on longitudinal cryosections (12 μm) for 60 minutes at room temperature. The sections were then washed 3 times with deionized water, dehydrated in a series of ascending alcohols, cleared with xylene, and mounted using Permount (Fisher).

Fluorescence in-situ hybridization

Fluorescence *in situ* hybridization on sciatic nerve sections was performed using the QuantiGene ViewRNA Tissue 2-Plex Assay kit (Affymetrix) according to the munfacturer's instructions. For detection of LKB1 transcripts a type 1 probe set was designed by Affymetrix corresponding to the bases 304–1368 of NM_011492. For detection of myelin basic protein (MBP) transcripts a type 6 probe set was designed (corresponding to the bases 17–2045 of NM_010777).

Quantification of dorsal root ganglion neurons

Expression of the *Thy1.2-YFP-16* transgene results in YFP-labelling of all mouse DRG neurons[54] allowing accurate quantification of neuronal cell body numbers. Entire dorsal root ganglia (L1-L5) were dissected from control LKB1$^{fl/fl}$(Thy1.2-YFP-16) and mutant LKB1$^{fl/fl}$: P0Cre+(Thy1.2-YFP-16) mice, cleaned from connective tissue, and mounted on glass slides. Neuronal cell body numbers per DRG were determined by a masked investigator using the ImageJ software cell-counter plug-in and manual counting.

Microscopic nerve imaging

We used a Nikon Eclipse 80i or Nikon Eclipse TE300 microscope system coupled to a digital camera (CoolSnapES[2]; Photometrics) for presentation of images from frozen and plastic semithin sections, or phase-contrast images from neuronal culture experiments. Confocal imaging was performed using a Zeiss LSM5 Pascal confocal system and Zeiss Confocal Software.

Electron micrographs of ultrathin sections were taken with Hitachi H-7500 or JEOL TEM 1200 EX II transmission electron microscopes.

Quantitative real-time PCR

Nerve RNA was extracted using the Zymo Research DNA-Free RNA Kit according to the manufacturer's recommendations. The nerve RNA was treated with DNAse (RQ1 Promega) and a no-RT control ensured absence of genomic DNA contamination. qRT-PCR for quantification of gene transcripts in sciatic nerves was performed as described previously[63] using a SYBR green-based assay on an ABI 7900 HT sequence detection system (Applied Biosciences). For each individual transcript, expression data from at least 3 LKB1^{fl/fl} control and 3 age-matched LKB1-SCKO mutant mice was obtained and normalized to glyceraldehyde-3-phosphate dehydrogenase (GAPDH) expression. Primers were as follows: GAPDH forward: TGCCCCCATGTTTGTGATG; GAPDH reverse: TGTGGTCATGAGCCCTTCC; LKB1 forward: GGGTCACACTTTACAACATCAC; LKB1 reverse: CGGCTCATACTCCAACATCC; Glut1 forward: GCTGTGCTTATGGGCTTCTC; Glut1 reverse: CACATACATGGGCACAAAGC; Glut3 forward: ATGGGGACAACGAAGGTGAC; Glut3 reverse: GTCTCAGGTGCATTGATGACTC; Glut4 forward: ACATACCTGACAGGGCAAGG; Glut4 reverse: CGCCCTTAGTTGGTCAGAAG. MCT1 forward: ATCGCAGGTGGCATTTTAAG; MCT1 reverse: GTCACGCATACTCCGGGC; MCT2 forward: GCTCTATCACGCTGTTGCTG; MCT2 reverse: GCTAGCTGTCATGTATGCGG; MCT4 forward: TCACGGGTTTCTCCTACGC; MCT4 reverse: GCCAAAGCGGTTCACACAC. Quantification of mitochondrial DNA content in sciatic nerves was performed as described previously[28].

Microarray and computational analysis

Sciatic nerves from P60 LKB1^{fl/fl} control (N=6 mice) and LKB1-SCKO mutant mice (N=6 mice) were dissected, cleaned from surrounding fat and connective tissue, and rapidly frozen in liquid nitrogen. Nerve RNA was extracted using a Qiagen mRNeasy Mini Kit according to the manufacturer's recommendations. Subsequent microarray analysis of nerve RNA using Illumina Mouse WG-6 v2.0 Expression Bead-chips was performed as described previously[6]. Probes having detection p-values > 0.05 in all samples were removed and a two class unpaired SAM analysis was performed. Differentially expressed genes with at least 2.0 fold differential regulation between control and LKB1-SCKO samples at a false discovery rate (FDR) of 2.5% were selected for analysis (presented in Supplementary Table 2). The Gene Expression Omnibus (GEO) accession number for the microarray data reported in this paper is GSE60325.

Measurement of metabolites in peripheral nerves and in cell culture media

For all metabolite measurements, sciatic nerves from LKB1^{fl/fl} control and age-matched LKB1-SCKO mutant mice were processed in parallel. For quantification of ATP, ADP, and NAD$^+$ concentrations, sciatic nerves were rapidly dissected, weighed, immediately placed in ice-cold perchloric acid (HClO$_4$) (10 volumes), and homogenized by sonication for 5 sec. After tissue pH neutralization (K$_2$CO$_3$) and centrifugation steps the extracts were analyzed using a Shimadzu HPLC system equipped with a LC-18T reverse-phase column (Supelco)

and quantification software (LabSolutions) as described previously[28]. The nucleotide concentrations were determined by measuring the absorbance at 254 nm and comparing to standards.

For quantification of sciatic nerve NAD^+/NADH ratios, weighed nerves from each mouse were divided for extract preparations in $HClO_4$ (for NAD measurement) and K_2CO_3 solutions (for NADH measurement) in parallel. After homogenization and centrifugation, nerve extracts were kept at 55°C for 15 min, incubated on ice, and pH neutralized. NAD^+/ NADH ratios in these extracts were determined using a fluorometric assay kit (BD Bioquest Enzo Works Fluirimetric NAD/NADH assay kit – red fluorescence) and a BMG Labtech Polarstar Optima fluorescence plate reader with attached analysis software.

For measurements of nerve glucose and lactate concentrations, sciatic nerves were rapidly dissected, weighed, and placed in ice-cold artificial cerebrospinal fluid (1x aCSF) buffer (10 volumes). Following homogenization and centrifugation, glucose and lactate concentrations in nerve extracts were measured using a YSI Life Sciences 2700 Select Biochemistry Analyzer equipped with D-Glucose and L-Lactate detection sensors.

Total cholesterol, tryglyceride, and fatty acid levels in sciatic nerves were determined using colorimetric assays with commercial detection reagents (Infinity Total Cholesterol and Infinity Triglycerides, Thermo Scientific; NEFA HR(2), Wako Chemicals). Snap-frozen sciatic nerves were weighed, homogenized in chloroform:methanol (2:1), and centrifuged at 12,000 rpm for 10 min at 4 °C. Aliquots for the respective measurements were evaporated in a microcentrifuge tube, the detection reagents added, and incubated at room temperature. The solutions were transferred to a 96-well plate with standards for chlolesterol/tryglyceride/ fatty acids, and the respective concentrations were determined with a plate reader following the manufacturer's instructions.

Measurement of lactate dehydrogenase enzyme activity in nerves

LDH enzyme activity in sciatic nerve homogenates was determined using a Lactate Dehydrogenase Activity Assay kit (Sigma) according to the manufacturer's instructions. In this assay, LDH reduces NAD^+ to NADH, which was specifically detected by a kinetic colorimetric measurement algorithm using a BMG Labtech Polarstar Optima plate reader and attached analysis software. Sciatic nerves were rapidly dissected from LKB1^{fl/fl} control and age-matched LKB1-SCKO mutant mice (at least 3 per genotype), weighed, and immediately placed in ice-cold LDH assay buffer. Nerves were homogenized by sonication for 10 sec, centrifuged, and an aliquot of the supernatant was used for the subsequent colorimetric measurement to determine LDH activity in milliunits/ml.

Nerve protein analysis and western blotting

Western blotting was performed using standard procedures as described previously[51,63]. Integrated band intensities of protein bands were measured using the ImageJ densitometry plug-in and normalized by comparison with the loading control (β-actin).

Tissue metabolite extraction for untargeted metabolomics

Sciatic nerves from P60 LKB1^{fl/fl} control (N=11 mice) and LKB1-SCKO mutant mice (N=11 mice) were dissected, cleaned from surrounding fat and connective tissue, and rapidly frozen in liquid nitrogen. Nerve tissues were lyophilized and normalized by mass prior to being extracted as previously described[67]. Lyophilized tissues were first treated with 600 μl of cold acetone, vortexed for 30 sec, incubated in liquid nitrogen for 1 min, and then sonicated for 10 min after being thawed at room temperature. This procedure was repeated three times. After an-hour incubation at −20 °C, samples were centrifuged for 10 min at 13,000 rpm and 4 °C. The resultant supernatant was transferred to a separate vial and kept at −20 °C. The remaining pellet was then treated with 400 & 956μl of cold methanol/water/ formic acid (86.5:12.5:1.0). After vortexing for 30 sec and sonicating for 15 min, the samples were stored at −20 °C for an hour. Samples were then centrifuged at 13,000 rpm for 10 min and the supernatant was collected. The supernatant was then pooled with that from the first extraction and dried by using a vacuum concentrator. After drying, each sample was either reconstituted in 100 & 956μl of acetonitrile/water (95:5) for nonpolar metabolites or in 100 & 956μl of methanol for polar metabolites.

Metabolomics LC/MS analysis and data processing with XCMS software

Each extracted sample was injected onto an HPLC column coupled to an Agilent 1200 series high performance liquid chromatography (HPLC) system. Two HPLC columns, reversed-phase C18 (RP-C18) column (Agilent ZORBAX SB-C18 column, 150 mm × 0.5 mm) and aminopropyl column (Phenomenex, 150 mm × 1.0 mm) were used to separate nonpolar and polar metabolites, respectively. The solvent system for RP liquid chromatography was water with 0.1% formic acid (mobile phase A) and acetonitrile with 0.1% formic acid (mobile phase B). The solvent gradient started from 2% B from 0–10 min, 10% B from 10–15> min, 20% B from 15–50 min, 95% B from 50–60 min and ended at 98% B.

The aminopropyl column was used in hydrophilic interaction (HILIC) mode with the following buffers: A = 95% water, 5% acetonitrile, 10mM ammonium hydroxide, 10mM ammonium acetate, pH 9.45; B = 95% acetonitrile, 5% water. The separations were done by using the following gradient: 100% B from 0–5 minutes, 100% to 0% B from 5–50 min, 0% B from 50–55. MS analysis was carried out on an Agilent 6520 Q-TOF with an electrospray ionization source in both positive and negative mode. All the MS1 spectra were collected with an acquisition rate of 1.02 spectra/sec with a mass range of 30–1500 mass units. The raw data files were converted into mzXML files using msconvert. The metabolite profiling analysis was performed on XCMS Online by using the centWave algorithm for features detection with peakwidth = 10–120 s and ppm = 20.

Nerve Lipidomics

Sciatic nerves from P60 LKB1^{fl/fl} control (N=3) and LKB1-SCKO mutant mice (N=3) were dissected, cleaned from surrounding fat and connective tissue, and rapidly frozen in liquid nitrogen. Nerve sample lipid extract preparations for mass spectrometry and subsequent analyses of lipid extracts by multi-dimensional mass spectrometry-based shotgun lipidomics was performed as described previously[6,68].

Schwann cell culture

Mouse sciatic nerves were rapidly dissected and placed in a sterile dish containing ice-cold DMEM. The nerve segments were freed of fat and connective tissue and coarsely teased into smaller fascicles using fine forceps. For dissociation of SCs the nerve tissue was treated with two sequential 15 min incubations at 37°C using solution 1 (Liberase TM 7 μg/ml, BSA 0.01 mg/ml, DNAse I 0.6 mg/ml) and solution 2 (Tripsin 0.05%), and was then triturated gently with a P1000 pipette. After brief centrifugation at 0.8g for 5 min, the final dissociated material was suspended in SC medium (DMEM, Bovine Pituitary Extract 2 μg/ml, Forskolin 2 μM, fetal bovine serum 10%, Peniccillin/Streptomycin) and seeded on polycarbonate FluoroDish cell culture dishes previously coated with poly-D-lysin (0.1 mg/ml) and laminin (0.01mg/ml). Degenerating axon portions and dead cells were washed out by frequent media washes. Ara-C (10 nM) was applied at DIV 2–3 to limit the growth of fibroblasts. The presence of PLP-EGFP fluorescence (from *PLP-EGFP* allele) or immunolabeling with S100 confirmed the presence of SCs at DIV 5–6.

Live-imaging of Schwann cell mitochondria

For imaging of SC mitochondria and their mitochondrial membrane potential or mitochondrial reactive oxygen species, primary SC cultures were loaded with following indicator dyes at DIV 5–6: MitoTracker Red CMXRos (250 nM, 10 min incubation); TMRM (Tetramethylrhodamine, methyl ester; 50 nm, 30 min incubation); MitoSOX Red (5 μM, 10 min incubation) (all Invitrogen). Following incubation, the cultures were washed with fresh medium and transferred into a live-imaging environmental chamber (5% CO_2, 37 °C) mounted on a Quorum Spinning disc Confocal/IX81-Olympus inverted microscope. Picture acquisition was performed using a 40x objective and Metamorph software. The mitochondrial indicator labeling was validated by addition of the mitochondrial uncoupler CCCP to the culture media. Fluorescence intensity in individual SCs was assessed using ImageJ as described previously[99]. Briefly, after confirmation of EGFP fluorescence (from *PLP-EGFP* allele), the area in each confocal micrograph occupied by SCs was defined using the ImageJ 'threshold' function, and the average red fluorescence intensity derived from the indicator dyes (MitoTracker RedCMXRos, TMRM, MitoSOX Red) was measured within this SC area. For each dye, SC cultures from sciatic nerves from 3 mice per genotype and examined age were used in 3 separate experiments. For each experiment we assessed fluorescence intensity in 10 microscopic field with ~40 cells. For high-resolution analysis of mitochondrial number and shape in individual SCs, Mitotracker Red CMXRos was additionally imaged after fixation with 4% PFA in PBS using a Nikon D-Eclipse C1 confocal microscope.

Lactate treatment of dorsal root ganglion (DRG) cultures

Dorsal root ganglia (DRGs) were dissected from E13.5 CD1 embryos and cultured as described previously[69]. DRG culture media containing lactate (Sigma) at the indicated concentrations was applied starting from DIV5, and changed every 24 hours to ensure constant levels for the following 8 days.

Nerve explant culture for measurement of lactate in culture media

Using sterile conditions sciatic nerves (~5 mm) were removed quickly from P60 LKB1^{fl/fl} control (N=3) and LKB1-SCKO mutant mice (N=3) that had been humanely killed. The nerve segments were transferred into ice-cold DMEM in a sterile dish. After removal of the perineurium, the nerves were cut into smaller segments, mechanically dissociated with a fine forceps, and transferred into a sterile 4-well dish containing 250 μl neurobasal media (Gibco) supplemented with fungizone. These preparations were then cultured in a humid atmosphere at 37°C, 5% CO_2. The conditioned medium was collected after 48 hr for quantification of lactate concentrations.

Nerve electrophysiology

Measurements of nerve conduction velocities and amplitudes of compound muscle action potentials (CMAPs) were performed as described previously[63].

Behavioral testing

Behavioral testing was performed using male and female SC-specific mutants and control littermates, or age-matched control animals with the appropriate genotypes. The experimenter was blind to the genotypes of the mice during data acquisition. Rotarod, hanging wire, and pole climb and turn tests were performed as previously described with minor modifications[63,70]. Standardized grip strength analysis of mouse anterior limbs was performed on a TSE Systems grip-strength meter (#303500) according to the manufacturer's instructions. Data are displayed as grip strength in ponds divided by the body weight of the experimental animal in kg.

Sensory analyses including Hargreaves, von Frey, and acetone tests were performed as described previously[28,63,70]. Exclusively female mice were used for these sensory tests. For the hot- and cold-pate tests female and male mice were placed on a Hot/Cold Plate analgesia meter (Ugo Basile) heated to 55 °C or 3 °C, respectively. The time it took the animals to start licking their forelimbs or to jump was recorded (time to pain reaction).

Antibodies

The primary and secondary antibodies used for nerve immunostaining and western blotting according to the manufacturer's recommendations are listed in Supplementary Table 4.

Statistical analysis and presentation of data

No statistical methods were used to pre-determine sample sizes but our sample sizes are similar to those reported in previous publications[6,28,63]. Data for all experiments were collected and processed randomly, but no formal randomization was carried out for this study. All demonstrated photomicrographs (immunolabeling, light and electron microscopy) are representative of at least 3 biological replicates. All quantitative data are presented as mean (± SEM) except in Box and Whisker plots (maximum, 25th percentile, median, 75th percentile, minimum). All statistical analyses were performed using Graph Pad Prism software (v6). A two-tailed Student's t-test was used for group comparisons and statistical significance was considered if $p < 0.05$.

Supplementary Material

Refer to Web version on PubMed Central for supplementary material.

Acknowledgments

References

1. Nave KA. Myelination and the trophic support of long axons. Nat Rev Neurosci. 2010; 11:275–283. [PubMed: 20216548]

2. Beirowski B. Concepts for regulation of axon integrity by enwrapping glia. Frontiers in cellular neuroscience. 2013; 7:256. [PubMed: 24391540]

3. Nave KA. Myelination and support of axonal integrity by glia. Nature. 2010; 468:244–252. [PubMed: 21068833]

4. Funfschilling U, et al. Glycolytic oligodendrocytes maintain myelin and long-term axonal integrity. Nature. 2012; 485:517–521. [PubMed: 22622581]

5. Lee Y, et al. Oligodendroglia metabolically support axons and contribute to neurodegeneration. Nature. 2012; 487:443–448. [PubMed: 22801498]

6. Viader A, et al. Aberrant schwann cell lipid metabolism linked to mitochondrial deficits leads to axon degeneration and neuropathy. Neuron. 2013; 77:886–898. [PubMed: 23473319]

7. Said G. Diabetic neuropathy–a review. Nat Clin Pract Neurol. 2007; 3:331–340. [PubMed: 17549059]

8. Eckersley L. Role of the Schwann cell in diabetic neuropathy. Int Rev Neurobiol. 2002; 50:293–321. [PubMed: 12198814]

9. Chowdhury SK, Smith DR, Fernyhough P. The role of aberrant mitochondrial bioenergetics in diabetic neuropathy. Neurobiol Dis. 2013; 51:56–65. [PubMed: 22446165]

10. Shackelford DB, Shaw RJ. The LKB1-AMPK pathway: metabolism and growth control in tumour suppression. Nat Rev Cancer. 2009; 9:563–575. [PubMed: 19629071]

11. Hardie DG, Ross FA, Hawley SA. AMPK: a nutrient and energy sensor that maintains energy homeostasis. Nat Rev Mol Cell Biol. 2012; 13:251–262. [PubMed: 22436748]

12. Lizcano JM, et al. LKB1 is a master kinase that activates 13 kinases of the AMPK subfamily, including MARK/PAR-1. EMBO J. 2004; 23:833–843. [PubMed: 14976552]

13. Bright NJ, Thornton C, Carling D. The regulation and function of mammalian AMPK-related kinases. Acta Physiol (Oxf). 2009; 196:15–26. [PubMed: 19245655]

14. Steinberg GR, Kemp BE. AMPK in Health and Disease. Physiol Rev. 2009; 89:1025–1078. [PubMed: 19584320]

15. Chowdhury SK, Dobrowsky RT, Fernyhough P. Nutrient excess and altered mitochondrial proteome and function contribute to neurodegeneration in diabetes. Mitochondrion. 2011; 11:845–854. [PubMed: 21742060]

16. Inoki K, Kim J, Guan KL. AMPK mTOR in Cellular Energy Homeostasis and Drug Targets. Annu Rev Pharmacol Toxicol. 2011

17. Shaw RJ. LKB1 and AMP-activated protein kinase control of mTOR signalling and growth. Acta Physiol (Oxf). 2009; 196:65–80. [PubMed: 19245654]

18. Barnes AP, et al. LKB1 and SAD kinases define a pathway required for the polarization of cortical neurons. Cell. 2007; 129:549–563. [PubMed: 17482548]

19. Granot Z, et al. LKB1 regulates pancreatic beta cell size, polarity, and function. Cell Metab. 2009; 10:296–308. [PubMed: 19808022]

20. Boehlke C, et al. Primary cilia regulate mTORC1 activity and cell size through Lkb1. Nat Cell Biol. 2010; 12:1115–1122. [PubMed: 20972424]

21. van der Velden YU, et al. The serine-threonine kinase LKB1 is essential for survival under energetic stress in zebrafish. Proc Natl Acad Sci U S A. 2011; 108:4358–4363. [PubMed: 21368212]

22. Contreras CM, et al. Loss of Lkb1 provokes highly invasive endometrial adenocarcinomas. Cancer Res. 2008; 68:759–766. [PubMed: 18245476]

23. Gan B, et al. Lkb1 regulates quiescence and metabolic homeostasis of haematopoietic stem cells. Nature. 2010; 468:701–704. [PubMed: 21124456]

24. Jessen N, et al. Ablation of LKB1 in the heart leads to energy deprivation and impaired cardiac function. Biochim Biophys Acta. 2010

25. Nakada D, Saunders TL, Morrison SJ. Lkb1 regulates cell cycle and energy metabolism in haematopoietic stem cells. Nature. 2010; 468:653–658. [PubMed: 21124450]

26. Patti GJ, Tautenhahn R, Siuzdak G. Meta-analysis of untargeted metabolomic data from multiple profiling experiments. Nat Protoc. 2012; 7:508–516. [PubMed: 22343432]

27. Chrast R, Saher G, Nave KA, Verheijen MH. Lipid metabolism in myelinating glial cells: lessons from human inherited disorders and mouse models. J Lipid Res. 2011; 52:419–434. [PubMed: 21062955]

28. Viader A, et al. Schwann cell mitochondrial metabolism supports long-term axonal survival and peripheral nerve function. J Neurosci. 2011; 31:10128–10140. [PubMed: 21752989]

29. Shorning BY, Clarke AR. LKB1 loss of function studied in vivo. FEBS Lett. 2011

30. Napoli I, et al. A central role for the ERK-signaling pathway in controlling Schwann cell plasticity and peripheral nerve regeneration in vivo. Neuron. 2012; 73:729–742. [PubMed: 22365547]

31. Arthur-Farraj PJ, et al. c-Jun reprograms Schwann cells of injured nerves to generate a repair cell essential for regeneration. Neuron. 2012; 75:633–647. [PubMed: 22920255]

32. Gwinn DM, et al. AMPK phosphorylation of raptor mediates a metabolic checkpoint. Mol Cell. 2008; 30:214–226. [PubMed: 18439900]

33. Corradetti MN, Inoki K, Bardeesy N, DePinho RA, Guan KL. Regulation of the TSC pathway by LKB1: evidence of a molecular link between tuberous sclerosis complex and Peutz-Jeghers syndrome. Genes Dev. 2004; 18:1533–1538. [PubMed: 15231735]

34. Lai LP, Lilley BN, Sanes JR, McMahon AP. Lkb1/Stk11 regulation of mTOR signaling controls the transition of chondrocyte fates and suppresses skeletal tumor formation. Proc Natl Acad Sci U S A. 2013; 110:19450–19455. [PubMed: 24218567]

35. Sherman DL, et al. Arrest of Myelination and Reduced Axon Growth When Schwann Cells Lack mTOR. J Neurosci. 2012; 32:1817–1825. [PubMed: 22302821]

36. Goebbels S, et al. Genetic disruption of Pten in a novel mouse model of tomaculous neuropathy. EMBO Mol Med. 2012; 4:486–499. [PubMed: 22488882]

37. Carling D, Sanders MJ, Woods A. The regulation of AMP-activated protein kinase by upstream kinases. Int J Obes (Lond). 2008; 32(Suppl 4):S55–59. [PubMed: 18719600]

38. Woods A, et al. Ca2+/calmodulin-dependent protein kinase kinase-beta acts upstream of AMP-activated protein kinase in mammalian cells. Cell Metab. 2005; 2:21–33. [PubMed: 16054096]

39. Herrero-Martin G, et al. TAK1 activates AMPK-dependent cytoprotective autophagy in TRAIL-treated epithelial cells. EMBO J. 2009; 28:677–685. [PubMed: 19197243]

40. Momcilovic M, Hong SP, Carlson M. Mammalian TAK1 activates Snf1 protein kinase in yeast and phosphorylates AMP-activated protein kinase in vitro. J Biol Chem. 2006; 281:25336–25343. [PubMed: 16835226]

41. Shackelford DB, et al. LKB1 inactivation dictates therapeutic response of non-small cell lung cancer to the metabolism drug phenformin. Cancer Cell. 2013; 23:143–158. [PubMed: 23352126]

42. Jaleel M, et al. Identification of the sucrose non-fermenting related kinase SNRK, as a novel LKB1 substrate. FEBS Lett. 2005; 579:1417–1423. [PubMed: 15733851]

43. Sun X, Gao L, Chien HY, Li WC, Zhao J. The regulation and function of the NUAK family. J Mol Endocrinol. 2013; 51:R15–22. [PubMed: 23873311]

44. Obrosova IG, Fathallah L, Lang HJ, Greene DA. Evaluation of a sorbitol dehydrogenase inhibitor on diabetic peripheral nerve metabolism: a prevention study. Diabetologia. 1999; 42:1187–1194. [PubMed: 10525658]

45. Stevens MJ, Obrosova I, Cao X, Van Huysen C, Greene DA. Effects of DL-alpha-lipoic acid on peripheral nerve conduction, blood flow, energy metabolism, and oxidative stress in experimental diabetic neuropathy. Diabetes. 2000; 49:1006–1015. [PubMed: 10866054]

46. Laden BP, Porter TD. Inhibition of human squalene monooxygenase by tellurium compounds: evidence of interaction with vicinal sulfhydryls. J Lipid Res. 2001; 42:235–240. [PubMed: 11181753]

47. Hofmeijer J, Franssen H, van Schelven LJ, van Putten MJ. Why are sensory axons more vulnerable for ischemia than motor axons? PLoS One. 2013; 8:e67113. [PubMed: 23840596]

48. Ramji N, Toth C, Kennedy J, Zochodne DW. Does diabetes mellitus target motor neurons? Neurobiol Dis. 2007; 26:301–311. [PubMed: 17337195]

49. Zochodne DW, Verge VM, Cheng C, Sun H, Johnston J. Does diabetes target ganglion neurones? Progressive sensory neurone involvement in long-term experimental diabetes. Brain. 2001; 124:2319–2334. [PubMed: 11673332]

50. Schmidt RE. Neuropathology and pathogenesis of diabetic autonomic neuropathy. Int Rev Neurobiol. 2002; 50:257–292. [PubMed: 12198813]

51. Babetto E, Beirowski B, Russler EV, Milbrandt J, DiAntonio A. The Phr1 ubiquitin ligase promotes injury-induced axon self-destruction. Cell Rep. 2013; 3:1422–1429. [PubMed: 23665224]

52. Bardeesy N, et al. Loss of the Lkb1 tumour suppressor provokes intestinal polyposis but resistance to transformation. Nature. 2002; 419:162–167. [PubMed: 12226664]

53. Feltri ML, et al. P0-Cre transgenic mice for inactivation of adhesion molecules in Schwann cells. Ann N Y Acad Sci. 1999; 883:116–123. [PubMed: 10586237]

54. Feng G, et al. Imaging neuronal subsets in transgenic mice expressing multiple spectral variants of GFP. Neuron. 2000; 28:41–51. [PubMed: 11086982]

55. Mallon BS, Shick HE, Kidd GJ, Macklin WB. Proteolipid promoter activity distinguishes two populations of NG2-positive cells throughout neonatal cortical development. J Neurosci. 2002; 22:876–885. [PubMed: 11826117]

56. Doerflinger NH, Macklin WB, Popko B. Inducible site-specific recombination in myelinating cells. Genesis. 2003; 35:63–72. [PubMed: 12481300]

57. Rodriguez CI, et al. High-efficiency deleter mice show that FLPe is an alternative to Cre-loxP. Nat Genet. 2000; 25:139–140. [PubMed: 10835623]

58. Dasgupta B, et al. The AMPK beta2 Subunit Is Required for Energy Homeostasis during Metabolic Stress. Mol Cell Biol. 2012; 32:2837–2848. [PubMed: 22586267]

59. Viollet B, et al. The AMP-activated protein kinase alpha2 catalytic subunit controls whole-body insulin sensitivity. J Clin Invest. 2003; 111:91–98. [PubMed: 12511592]

60. Jorgensen SB, et al. Knockout of the alpha2 but not alpha1 5′-AMP-activated protein kinase isoform abolishes 5-aminoimidazole-4-carboxamide-1-beta-4-ribofuranosidebut not contraction-induced glucose uptake in skeletal muscle. J Biol Chem. 2004; 279:1070–1079. [PubMed: 14573616]

61. Lesche R, et al. Cre/loxP-mediated inactivation of the murine Pten tumor suppressor gene. Genesis. 2002; 32:148–149. [PubMed: 11857804]

62. Viader A, Chang LW, Fahrner T, Nagarajan R, Milbrandt J. MicroRNAs modulate Schwann cell response to nerve injury by reinforcing transcriptional silencing of dedifferentiation-related genes. J Neurosci. 2011; 31:17358–17369. [PubMed: 22131398]

63. Beirowski B, et al. Sir-two-homolog 2 (Sirt2) modulates peripheral myelination through polarity protein Par-3/atypical protein kinase C (aPKC) signaling. Proc Natl Acad Sci U S A. 2011; 108:E952–961. [PubMed: 21949390]

Author Manuscript   Author Manuscript   Author Manuscript   Author Manuscript

64. Beirowski B, et al. Non-nuclear Wld(S) determines its neuroprotective efficacy for axons and synapses in vivo. J Neurosci. 2009; 29:653–668. [PubMed: 19158292]

65. Mack TG, et al. Wallerian degeneration of injured axons and synapses is delayed by a Ube4b/Nmnat chimeric gene. Nat Neurosci. 2001; 4:1199–1206. [PubMed: 11770485]

66. Hunter DA, et al. Binary imaging analysis for comprehensive quantitative histomorphometry of peripheral nerve. J Neurosci Methods. 2007; 166:116–124. [PubMed: 17675163]

67. Yanes O, Tautenhahn R, Patti GJ, Siuzdak G. Expanding coverage of the metabolome for global metabolite profiling. Anal Chem. 2011; 83:2152–2161. [PubMed: 21329365]

68. Yang K, Cheng H, Gross RW, Han X. Automated lipid identification and quantification by multidimensional mass spectrometry-based shotgun lipidomics. Anal Chem. 2009; 81:4356–4368. [PubMed: 19408941]

69. Miller BR, et al. A dual leucine kinase-dependent axon self-destruction program promotes Wallerian degeneration. Nat Neurosci. 2009; 12:387–389. [PubMed: 19287387]

70. Golden JP, et al. RET signaling is required for survival and normal function of nonpeptidergic nociceptors. J Neurosci. 2010; 30:3983–3994. [PubMed: 20237269]
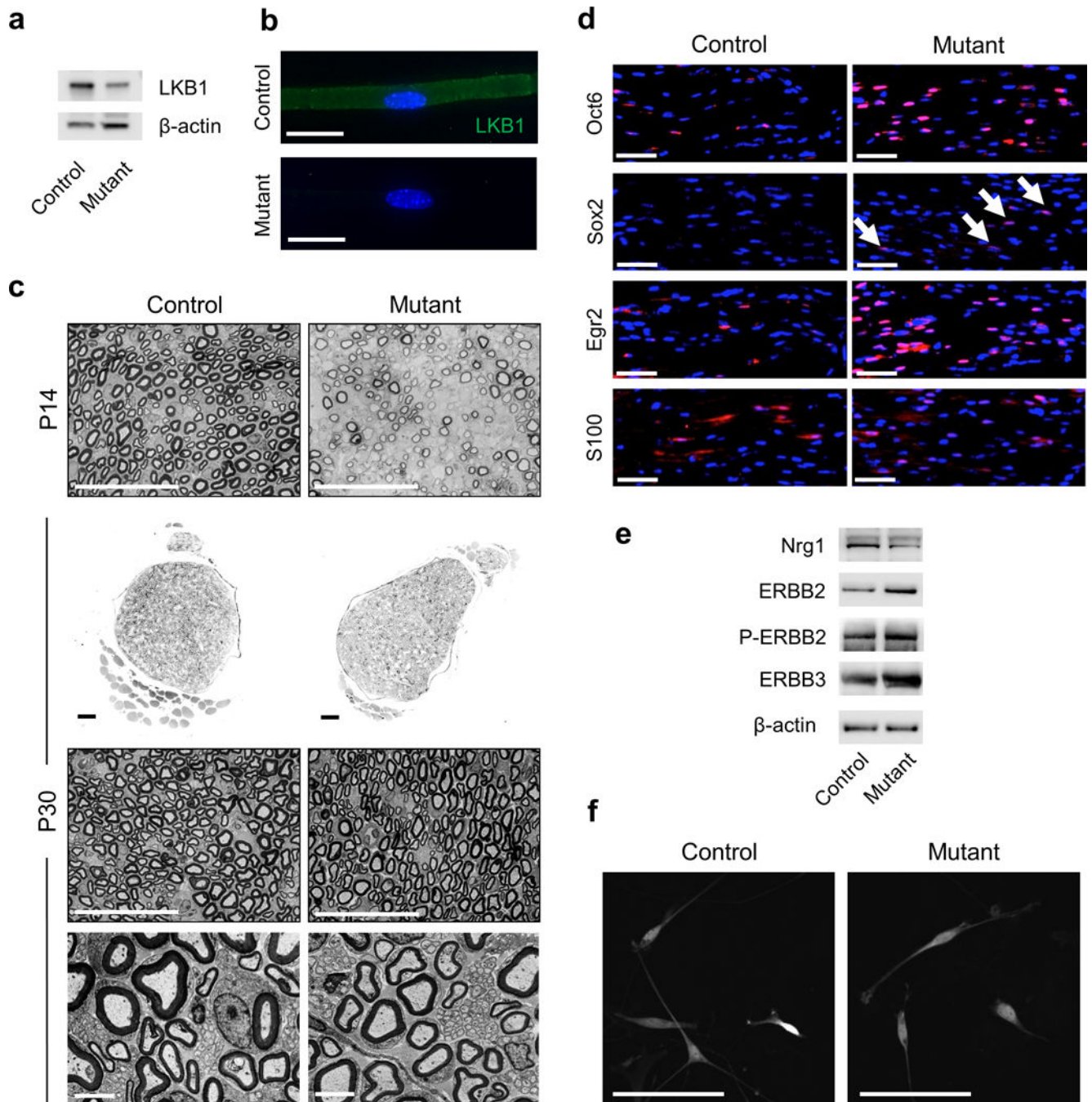
Figure 1.

Conditional deletion of LKB1 in SCs.

(a) Western blots of sciatic nerve lysates from P30 LKB1^{fl/fl} control and LKB1-SCKO mouse probed with the indicated antibodies shows marked reduction of LKB1 protein expression in the mutant.

(b) Fluorescence immunolabeling on teased fiber preparations from P30 tibial nerves demonstrating strong reduction of LKB1 protein in the LKB1-SCKO sample as compared to LKB1^{fl/fl} control. Blue: DAPI, scale bars: 20 μm

(c) Representative light and electron micrographs (bottom panel) of transverse sciatic nerve sections from LKB1$^{fl/fl}$ control and LKB1-SCKO mice at the indicated ages. Note substantial hypomyelination at P14 in mutant nerves that is no longer apparent at P30. Scale bars: 40 μm (light microscopy), 2 μm (electron microscopy).

(d) Immunofluorescence of longitudinal frozen sciatic nerve (P21) sections using the indicated stage-specific markers shows marked increases in SCs expressing Oct6, Sox2 (arrows), and Egr2 in LKB1-SCKO nerves as compared to LKB1$^{fl/fl}$ control nerves, while there is no difference in the number of S100-positive SCs. Blue: DAPI, scale bars: 50 μm

(e) Western blots of sciatic nerve lysates from P30 LKB1$^{fl/fl}$ control and LKB1-SCKO mouse probed with the indicated antibodies shows reduction of the active fragment of axonal Nrg1 expression in the mutant nerve, and concomitant increase of ERBB2, phospho-ERBB2, and ERBB3 signals.

(f) Representative confocal fluorescence microscopy of primary SC cultures established from P30 sciatic nerves from control (LKB1$^{fl/fl}$:PLP-EGFP) and mutant (LKB1$^{fl/fl}$:P0Cre +:PLP-EGFP) mouse shows no obvious structural differences between individual SCs from each genotype. Scale bars: 100 μm

For uncropped pictures of western blots see Supplementary Figure 19.
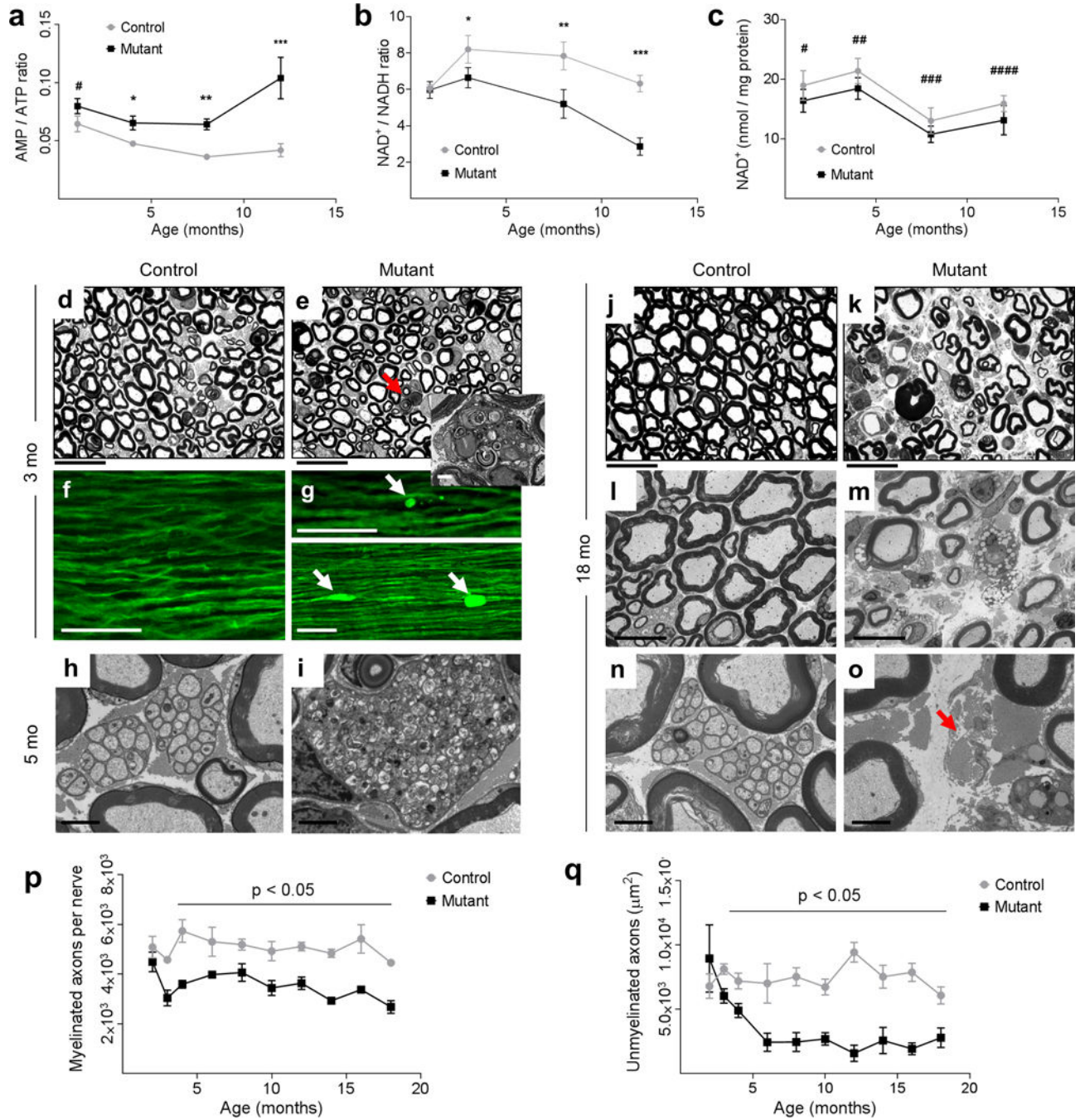
Figure 2.
Metabolic alterations and progressive axonopathy in LKB1-SCKO nerves.
(a–c) Increased AMP/ATP (a) and reduced NAD^+/NADH ratios (b) in sciatic nerve preparations from LKB1-SCKO mutants as compared to LKB1$^{fl/fl}$ control mice. Note no significant differences in sciatic nerve NAD^+ levels (c). a: $^{\#}P=0.130$ (N=7), $^{*}P=0.021$ (N= 6–7), $^{**}P<0.001$ (N=6), $^{***}P=0.010$ (N=6–7); b: $^{*}P=0.034$ (N=4–5), $^{**}P=0.008$ (N=6), $^{***}P<0.001$ (N=5); c: $^{\#}P=0.431$ (N=7), $^{\#\#}P=0.312$ (N=6–7), $^{\#\#\#}P=0.399$ (N=6), $^{\#\#\#\#}P=0.361$ (N=7). N indicates mice per genotype

(d–o) Light (d, e, j, k), electron (h, i, l–o), and confocal microscopy (f, g) of sciatic nerves from control (LKB1$^{fl/fl}$[Thy1.2-YFP-16]) and mutant (LKB1$^{fl/fl}$:P0Cre+[Thy1.2-YFP-16]) mice at the indicated ages. Collapsed or fragmented profiles of myelinated axons appeared initially in P90 LKB1-SCKO samples (arrow in e, inset shows example electron micrograph of degenerated axon), and became abundant in aged mutants (k, m). Note numerous fiber ovoids, and reduced axon density with increased inter-axonal spaces (k, m). Longitudinal axoplasm imaging revealed axonal continuity interruption and swelling (g). Degeneration of unmyelinated axons occurred in Remak bundles by initial disintegration/swelling (i) and later complete loss (o, arrow). Scale bars: 20 μm (d, e, j, k); 2 μm (inset in e); 50 μm (f, g); 2 μm (h, i, n, o); 10 μm (l, m)

(p, q) Quantification of myelinated (p) and unmyelinated axons (q) in sciatic nerves from LKB1$^{fl/fl}$ control and LKB1-SCKO mice from 2–18 months of age. Note significant loss of both axon populations in mutants starting at 3 months of age. N=4–7 mice per genotype at each age
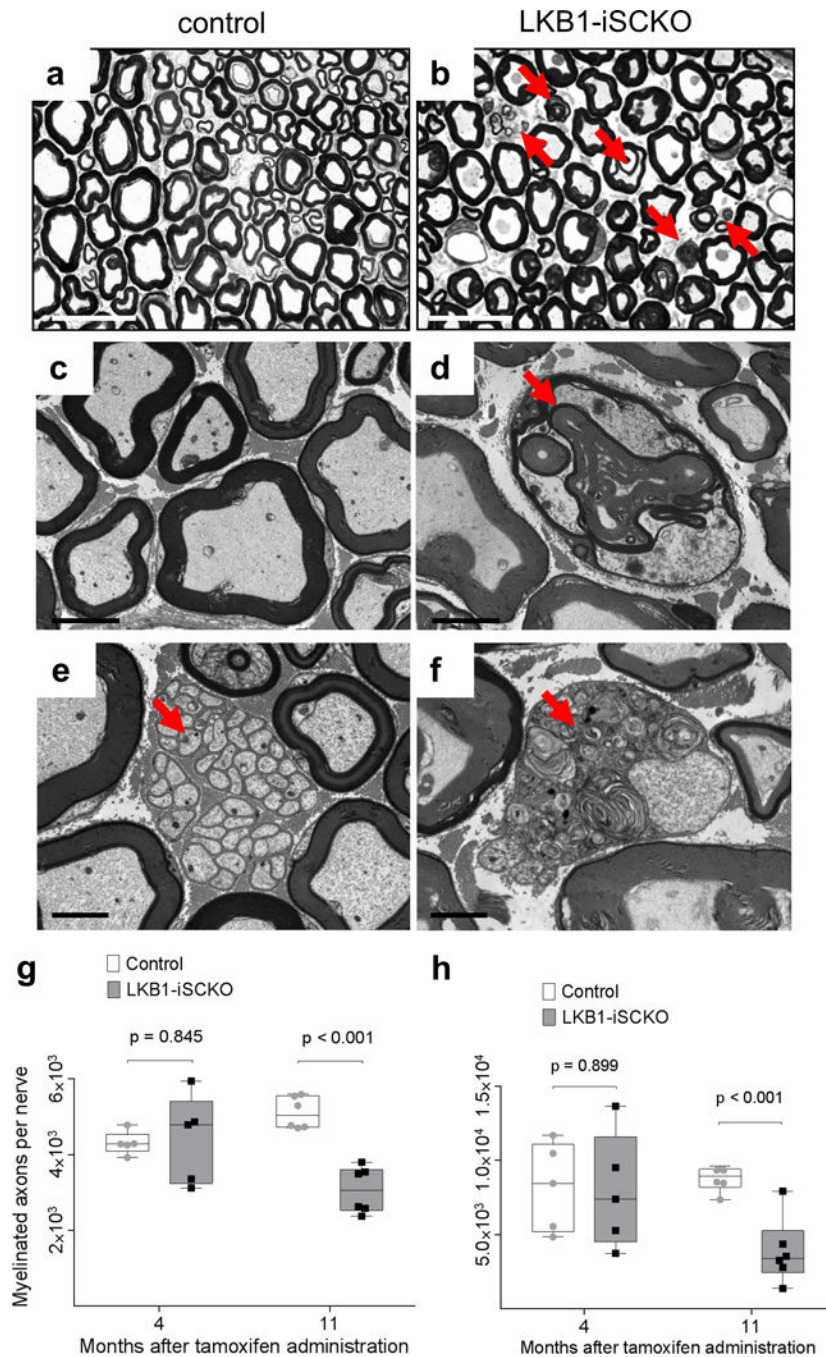
Figure 3.
Axon degeneration in LKB1-iSCKO mutants.

(a–f) Light (a, b), and electron microscopy (c–f) of transverse sciatic nerve sections from 12-month-old LKB1$^{fl/fl}$ control mice (a, c, e) and LKB1$^{fl/fl}$: PLP-Cre^{ERT} (LKB1-iSCKO) mutants that were treated with tamoxifen starting at P30 (b, d, f).

Arrows indicate degenerated profiles of mutant myelinated axons (b, d) and unmyelinated Remak fibers (f). Scale bars: 20 μm (a, b), 4 μm (c, d), 2 μm (e, f)

(g, h) Quantification of myelinated (g) and unmyelinated axons (h) in sciatic nerves from LKB1$^{fl/fl}$ control and LKB1-iSCKO mice at 4 and 11 months after tamoxifen administration shows significant reductions in axon numbers in LKB1-iSCKO mutants. N=5–6 mice per genotype at each time-point
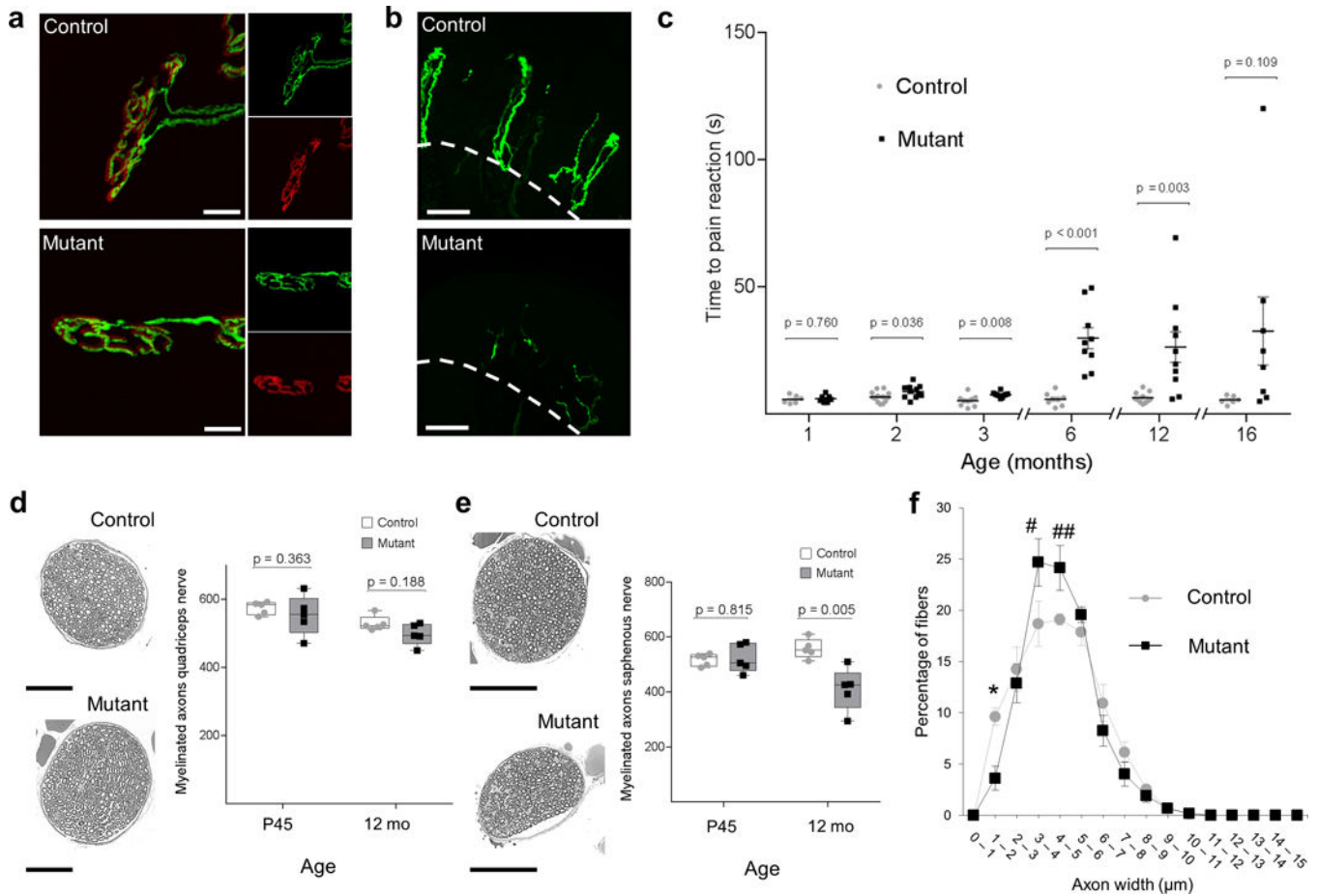
Figure 4.
Preservation of motor and loss of sensory axons in LKB1-SCKO mutants.

(a) Confocal z-series projections of extensor hallucis longus (EHL) whole-mount muscle preparations from 16-month-old LKB1$^{fl/fl}$(Thy1.2-YFP-16) control and LKB1-SCKO(Thy1.2-YFP-16) mice. Green: YFP; red: TRITC-α-bungarotoxin. Note co-localization of green axon terminals and red postsynaptic signals indicating preserved neuromuscular junctions in mutant mice. Scale bars: 20 μm

(b) Confocal z-series projections of intraepidermal sensory axon terminals in footpads from 12-months-old LKB1$^{fl/fl}$(Thy1.2-YFP-16) control and LKB1-SCKO(Thy1.2-YFP-16) mutant show almost complete axon degeneration in the mutant. The dotted lines depict the border between dermis and epidermis. Scale bars: 20 μm

(c) Graph showing results of hot-plate tests for mouse cohorts at the indicated ages. Note significantly increased reaction latencies to thermal pain stimulus in mutants from 2–16 months of age.

(d, e) Light microscopy (at 12 months of age) and quantification of motor and sensory myelinated axons in quadriceps (d) and saphenous nerves (e) at the indicated ages. Note reduced nerve size and axon numbers in mutant saphenous nerves, but no differences in quadriceps nerves from 12-month-old mice. Scale bars: 100 μm

(f) Axon width distribution profile in sciatic nerves from 8-month-old mice.
*P=0.003, #P=0.096, ##P=0.055, N=5 mice per genotype
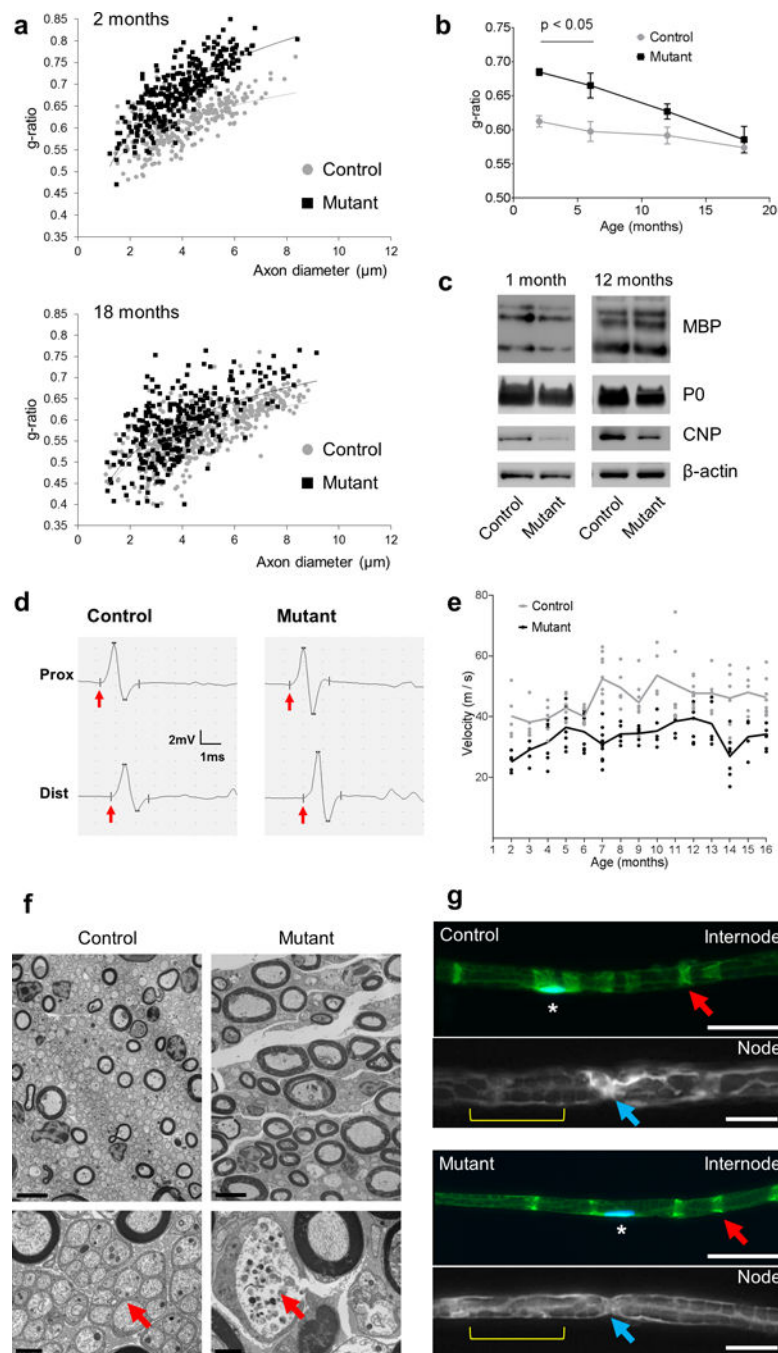
Figure 5.
Absence of demyelination in LKB1-SCKO mutants.

(a, b) Sciatic nerve g-ratios as a function of axon diameter (a). Note improvement of g-ratio deficits as LKB1-SCKO mutants age (b) (N=3–5 mice per genotype and age). N=3–5 mice per genotype and age

(c) Representative western blots (from at least 5 independent experiments) of sciatic nerve lysates probed with the indicated antibodies for detection of structural myelin proteins. For uncropped pictures of western blots see Supplementary Figure 19.

(d) Traces of sciatic nerve CMAPs recorded from a foot muscle after proximal and distal stimulation in 12-month-old mice. Arrows indicate the onset of the CMAPs. Compared to controls, mutants display slightly prolonged latencies, but there is no temporal dispersion of the CMAPs.

(e) Quantification of nerve conduction velocities. Each data point represents the mean of 2 measurements per mouse (left and right hind limb), and continuous lines indicate means for each genotype. N=5–10 mice per genotype and age

(f) Electron microscopy of transverse vagus nerve sections from 13-month-old mice. Note prominent degeneration of mutant unmyelinated fibers (red arrows) with swollen and disintegrated axoplasm while myelinated large diameter fibers appear relatively intact in the mutant. Scale bars: 4 μm (overview), 1 μm (high magnification)

(g) Teased fiber preparations from 14-month-old LKB1$^{fl/fl}$:PLP-EGFP control and LKB1-SCKO:PLP-EGFP mutant mice showing internodal portions with SC nuclei (asterisks) and nodal segments. Note normal appearance of Schmidt-Lanterman incisures (red arrows), nodes of Ranvier (blue arrows), and longitudinal and transverse Cajal bands (cytoplasmic channels depicted by yellow brackets) in mutant. Scale bars: 20 μm (internode); 4 μm (node)
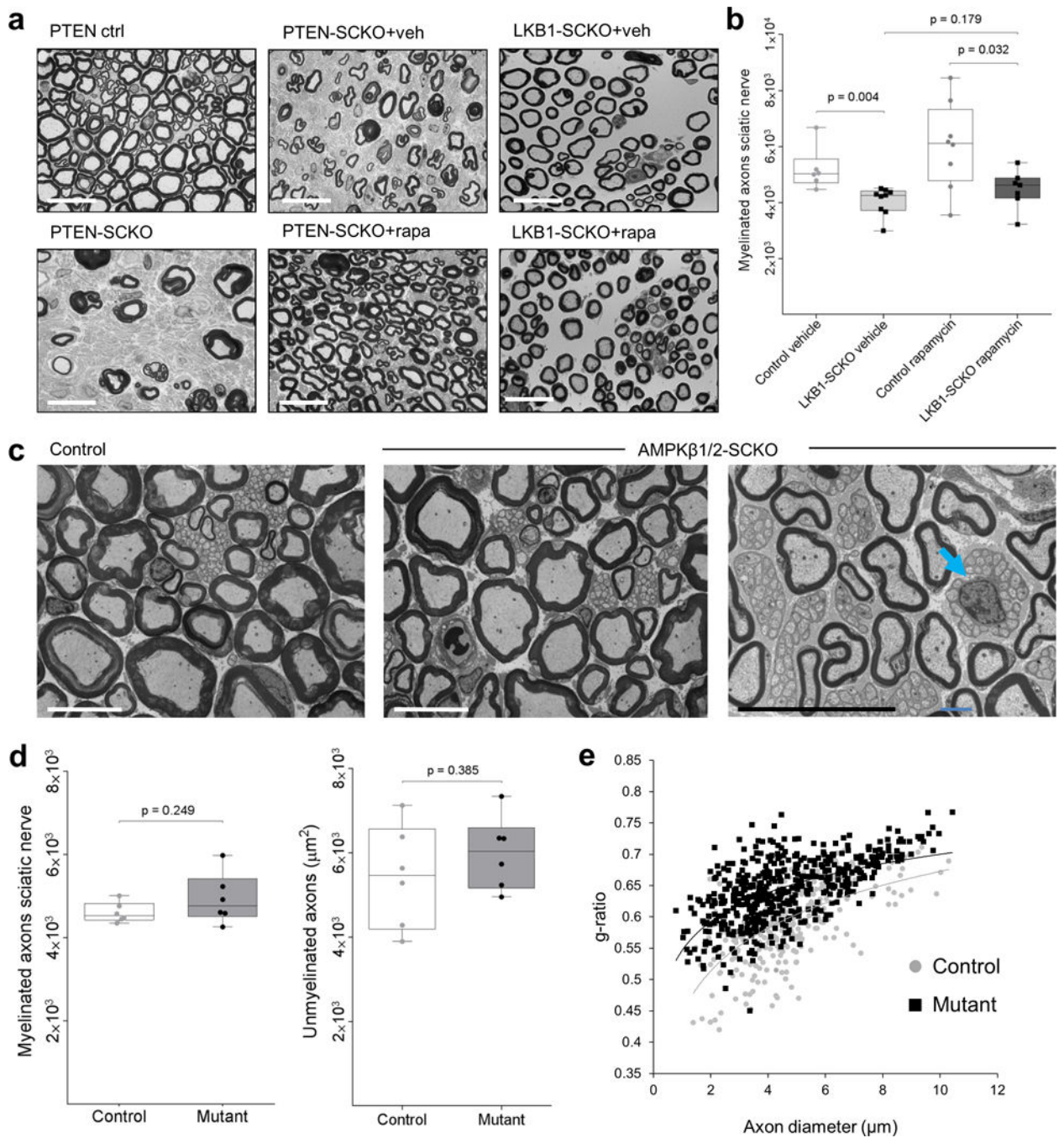
Figure 6.
Direct perturbation of AMPK in SCs does not cause axon losses.
(a) Light micrographs of sciatic nerves from untreated PTEN^{fl/fl} control and PTEN-SCKO (both 11 months) (left column), and rapamycin (rapa) or vehicle (veh) treated PTEN^{fl/fl} control, PTEN-SCKO, and LKB1-SCKO mice (all P90). Note substantially improved nerve integrity with higher axon density in PTEN-SCKO mutants treated with rapamycin for 60 days as compared to vehicle treated mutants (middle column). There is no improvement in

nerve integrity or a reduction in axon losses in rapamycin-treated LKB1-SCKO mice (right column). Scale bar: 20 μm

(b) Quantification of myelinated sciatic nerve axons from P90 LKB1^{fl/fl} control and LKB1-SCKO mice following 60 days of vehicle or rapamycin treatment.

(c) Electron microscopy of sciatic nerve transverse sections from 18-month-old control and AMPKβ1/2-SCKO mutants. Note hypomyelination, but normal axon structure and Remak bundle configuration (example depicted by blue arrow) in mutant. Scale bars: 10 μm

(d) Quantification of axon populations in sciatic nerves from 12-month-old control and AMPKβ1/2-SCKO mice shows no difference in total axon numbers. N=6 mice per genotype

(e) Sciatic nerve fiber g-ratios are shown as a function of axon diameter in 12-month-old control and AMPKβ1/2-SCKO mice. Note the increased g-ratio in these animals, indicative of hypomyelination. N=3–5 mice per genotype
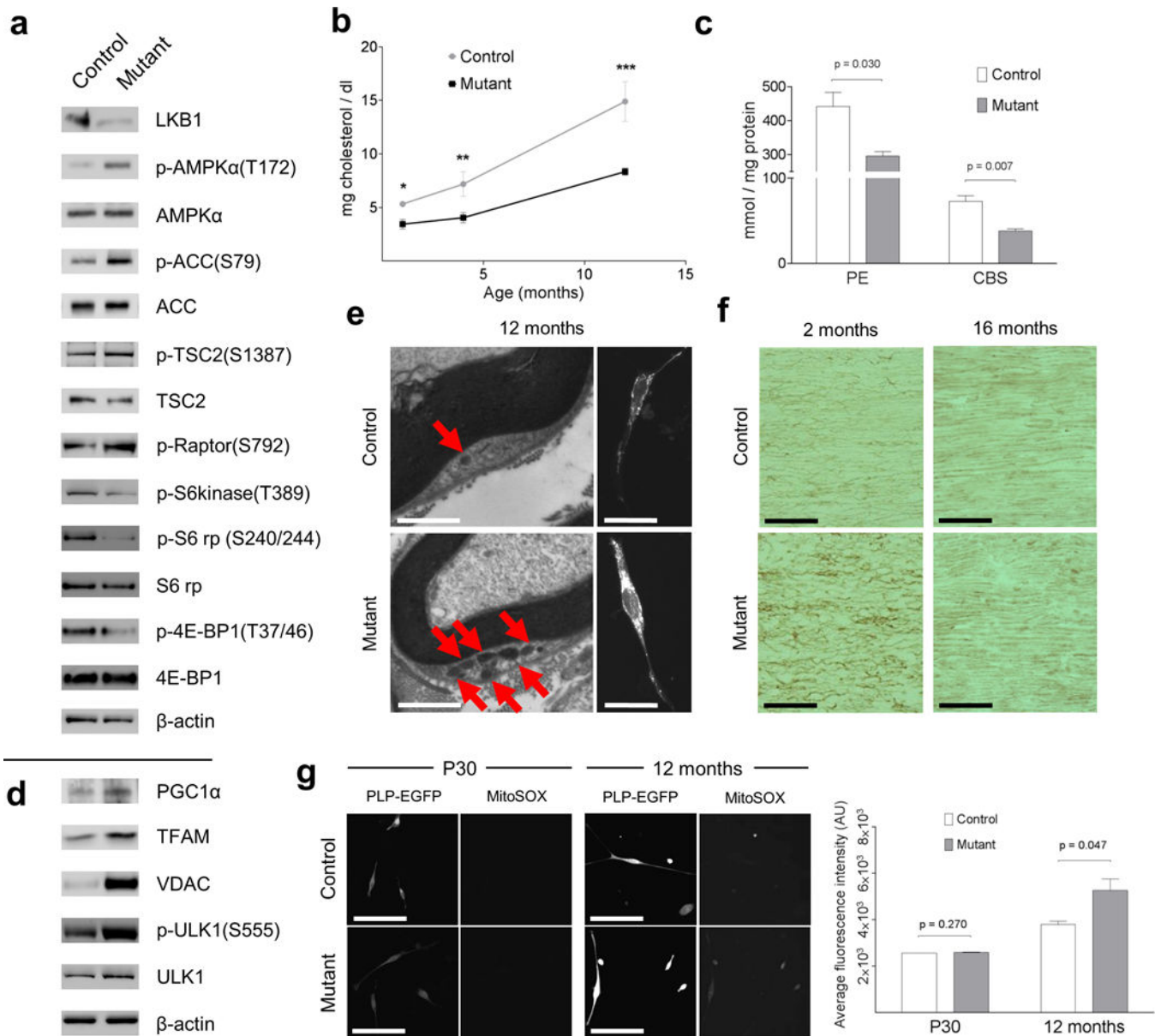
Figure 7.
Characterization of downstream pathways and mitochondria in LKB1-SCKO nerves.

(a) Western blot analysis of P30 sciatic nerve protein extracts using the indicated antibodies shows pathway alterations consistent with increased AMPK activity.

(b) Decreased relative levels of cholesterol in lipid extracts from mutant sciatic nerves at the indicated ages. *P=0.002, **P=0.035, ***P<0.038; N=3–7 mice per genotype and age

(c) Nerve lipidomic analysis shows decreased concentrations of total phosphatidylethanolamine lipids (PE) and total cerebrosides (CBS). N=3 mice per genotype

(d) Western blots of P30 sciatic nerve lysates probed with the indicated antibodies show increased mitochondrial burden in LKB1-SCKO nerves.

(e) Left: Electron micrograph showing increased numbers of mitochondria (red arrows) in SC cytoplasm of LKB1-SCKO nerve (12 months). Scale bars: 1 μm

Right: Confocal microscopy of cultured SCs (paraformaldehyde fixed preparations) from 12-month-old control and mutant mouse treated with MitoTracker Red CMXRos shows increased mitochondrial staining intensity in the mutant SC. Scale bars: 25 μm

(f) Cytochrome oxidase enzymatic staining of longitudinal sciatic nerve sections shows increased mitochondrial activity in nerves of LKB1-SCKO mice at 2 months, but not at 16 months. Scale bars: 100 μm

(g) Confocal live-cell imaging analysis of primary SC cultures loaded with the mitochondrial superoxide indicator dye MitoSOX Red from P30 and 12-month-old mice. Graphs depict average cumulative fluorescence intensities (AU: arbitrary units) of MitoSOX Red signal in SCs. Note significantly increased mitochondrial ROS signals in SCs from 12-month-old mutant mice. N=3 mice per genotype. Scale bars: 100 μm

Western blot data are representative for results obtained from at least 5 mice per genotype. For uncropped pictures see Supplementary Figure 19.
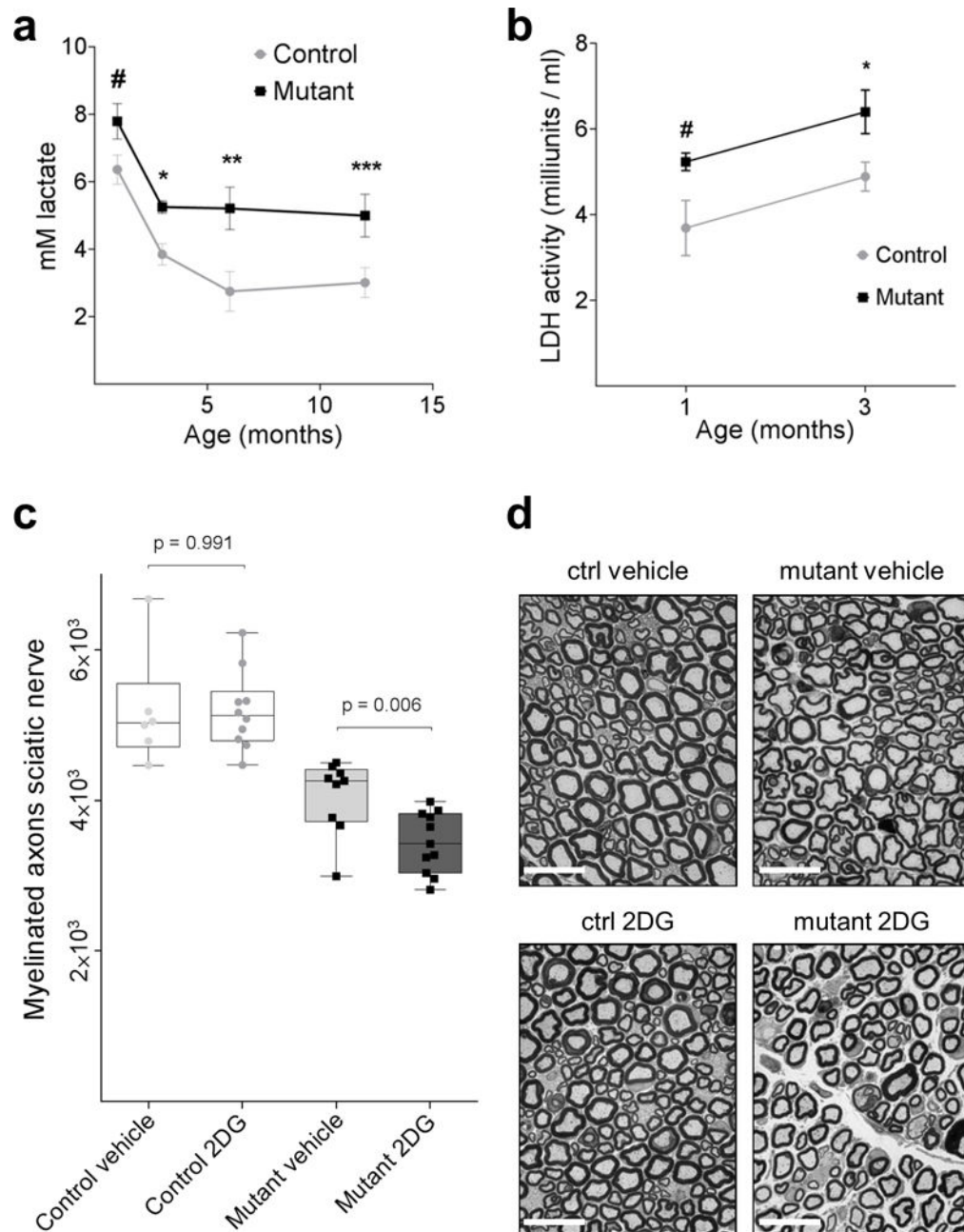
Figure 8.
Augmented lactate release in LKB1-SCKO nerves supports axonal maintenance.

(a) Increased lactate levels in LKB1-SCKO sciatic nerve preparations at 3 months of age and onwards. [#]P=0.087, *P=0.019, **P=0.045, ***P=0.027; N=3–6 mice per genotype and age

(b) Increased lactate dehydrogenase (LDH) activity in sciatic nerve preparations from 3-month-old LKB1-SCKO mutants. [#]P=0.084, *P=0.039; N=3–5 mice per genotype and age.

(c) Reduced sciatic nerve axon numbers in 2DG-treated versus vehicle-treated LKB1-SCKO mutants. Long-term 2DG administration had no effect in control nerves. N=6–11 mice per group

(d) Light micrographs of sciatic nerves from vehicle- and 2DG-treated P90 mice. Scale bar: 20 μm